Early to Middle Miocene Astronomically-Paced Climate Dynamics in the Eastern Equatorial Atlantic

Bianca R. Spiering[1], Evi Wubben[1], Frederik J. Hilgen[1], and Appy Sluijs[1]

[1]Department of Earth Sciences, Faculty of Geosciences, Utrecht University, Utrecht, The Netherlands.

Corresponding author: Bianca Spiering (b.r.spiering@uu.nl)

Key Points:

- The West African monsoon drove astronomically-paced variations in upwelling intensity, productivity, and dust supply between 18 and 15 Ma.
- 60-50 kyr cyclicity between 16.9 and 16.3 Ma resulted from precession-obliquity combination tones within a 2.4 Myr eccentricity minimum.
- Asymmetric eccentricity and obliquity cycles suggest an influence of high-latitude, glacial-interglacial variability.

Abstract

Detailed analysis of tropical climate dynamics is lacking for the Early to Middle Miocene, even though this time interval bears important analogies for future climates. Based on high-resolution proxy reconstructions of sea surface temperature, export productivity and dust supply at Ocean Drilling Program Site 959, we investigate astronomical forcing of the West African monsoon in the eastern equatorial Atlantic across the prelude, onset, and continuation of the Miocene Climatic Optimum (MCO; 18-15 Ma). Along with previously identified eccentricity periodicities of ~400 kyr and ~100 kyr, our records show that climate varied on ~27-17 kyr, ~41 kyr, and ~60-50 kyr timescales, which we attribute to precession, obliquity, and their combination tones, respectively. The relative contribution of these astronomical cycles differed between proxies and through time. Three intervals with distinct variability were recognized, which are particularly clear in the temperature record: (1) strong eccentricity, obliquity, and precession variability prior to the MCO (18.2-17.7 Ma), (2) strong influence of obliquity just after the onset of the MCO (16.9-16.3 Ma) concurring with a 2.4 Myr eccentricity minimum, and (3) dominant eccentricity and precession variability during the MCO between 16.3 and 15.0 Ma. Sedimentation at Site 959 was influenced by astronomically-paced variations in upwelling intensity and North African aridity related to West African monsoon dynamics. Continuously present patterns of precession imply low-latitude forcing, while asymmetric eccentricity and obliquity imprints and strong obliquity influence suggest that Site 959 was also affected by high-latitude, glacial-interglacial dynamics.

1 Introduction

The Miocene Climatic Optimum (MCO; ~17-15 Ma) was an interval of global warmth that interrupted the long-term Cenozoic cooling trend recognized in benthic foraminiferal oxygen isotope records (Vincent & Berger, 1985; Westerhold et al., 2020; Woodruff & Savin, 1991). Proxy reconstructions indicate that the MCO was significantly warmer than today (Burls et al., 2021) with atmospheric CO_2 of 400-600 ppm and possibly peak values up to 800-1100 ppm (Foster et al., 2012; Sosdian et al., 2018; Steinthorsdottir et al., 2019; Stoll et al., 2019; Super et al., 2018; Y.G. Zhang et al., 2013). These estimates are comparable to predictions for the near future, making the MCO an interesting analogue for future climate change (Steinthorsdottir et al., 2021). Continuous, high-resolution records for the Early to Middle Miocene are, however, limited to benthic foraminiferal stable carbon and oxygen isotope records describing deep-ocean and high-latitude environments (e.g., Holbourn et al., 2007; Holbourn et al., 2015; Liebrand et al., 2016), while high-resolution records on tropical (monsoon) dynamics are lacking.

The West African monsoon is one of Earth's regional monsoon systems that dominates hydrological cycling and zonal heat gradients in the Atlantic Ocean. Sediments from the Mediterranean Sea, the subtropical Atlantic off Northwest Africa, and the eastern equatorial Atlantic (Figure 1a) revealed that the West African monsoon responded strongly to astronomical forcing. Pleistocene to Late Miocene sapropel-marl deposits in the Mediterranean are widely acknowledged to reflect astronomically-forced variations between humid and dry North African climate states (e.g., Lourens et al., 2001; Rossignol-Strick, 1983; Schenau et al., 1999). Similarly, inferred wet-dry variations show an established West African monsoon off Northwest Africa for at least the past 11 Myr (Crocker et al., 2022; O'Mara et al., 2022; Tiedemann et al., 1994) and in the eastern equatorial Atlantic between 2 and 6 Ma (Vallé et al., 2017). Climate simulations (for <1 Ma) imply that the sedimentary observations are indeed consistent with the

response of the African monsoon to astronomical forcing through variability in atmospheric and hydrologic circulation (Bosmans, Drijfhout, et al., 2015; Bosmans, Hilgen, et al., 2015). Both sediments and models indicate that precession, which dominates insolation changes at low latitudes, was the main driver of monsoon variability (Bosmans, Drijfhout, et al., 2015).

Further back in time, Eocene, Paleocene, and Late Cretaceous sediments from the eastern equatorial Atlantic as well as Early Cretaceous sediments from the South Atlantic contain precession cycles in organic carbon content (Beckmann et al., 2005; Behrooz et al., 2018; Cramwinckel et al., 2018; Frieling et al., 2019). For the Cretaceous, these were ascribed to monsoonal wet-dry oscillations (Beckmann et al., 2005; Behrooz et al., 2018), although presumably operating differently from the modern system due to differences in the land-sea distribution (Beckmann et al., 2005). Interestingly, simulations suggest that modern West African monsoon circulation only developed during the mid-Cenozoic as the Atlantic basin expanded (Acosta et al., 2022). These simulations also suggest an intensification of the West African monsoon in response to an atmospheric CO_2-induced temperature increase (Acosta et al., 2022). Vegetation changes were also shown to influence the monsoon strength (Acosta et al., 2022). However, sedimentological observations of West African monsoon variability during the Early and Middle Miocene, including its response to the onset of the MCO, are lacking.

To address this knowledge gap, we investigate potentially monsoon-related astronomical cyclicity in the Early to Middle Miocene using sediments recovered at Ocean Drilling Program (ODP) Site 959 in the eastern equatorial Atlantic (Figure 1; Mascle et al., 1996). This site has previously been used to study monsoon variability in other time periods (Beckmann et al., 2005; Norris, 1998a; Vallé et al., 2017; Wagner, 1998, 2002). A recent age model for the Lower to Middle Miocene sediments showed that a near-complete 18-15 Ma section was recovered, suitable for assessing climate variability at precession to eccentricity timescales (Wubben et al., 2023). We use records of sediment color, magnetic susceptibility (MS), bulk carbonate stable carbon and oxygen isotopic composition ($\delta^{13}C$ and $\delta^{18}O$) and weight percent (wt%) $CaCO_3$ published in Wubben et al. (2023), biomarker paleothermometer data from a companion paper (Wubben et al., in press), as well as newly presented bulk sediment elemental composition data (biogenic Ba, Ti/Al, and V/Al). Detailed frequency analysis is performed on these high-resolution records to investigate the response to astronomical forcing across the prelude, onset, and continuation of the MCO. Subsequently, the nature of potential monsoon-forcing is evaluated on different astronomical timescales.

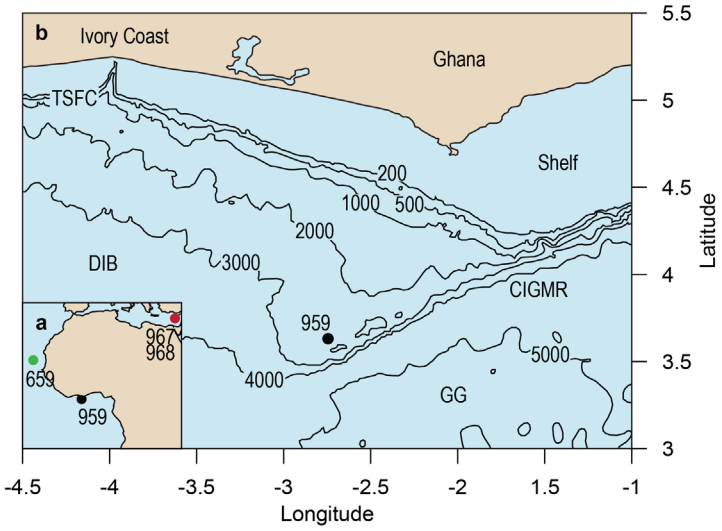

Figure 1. Location maps of Site 959: (**a**) map showing the position of Site 959 in the eastern equatorial Atlantic, Site 659 in the subtropical Atlantic off Northwest Africa, and Sites 967-968 in the eastern Mediterranean, and (**b**) bathymetric map of Site 959 with depth contour lines in meters. Bathymetry is based on data from GEBCO Bathymetric Compilation Group (2022). Abbreviations: CIGMR = Côte d'Ivoire-Ghana Marginal Ridge, DIB = Deep Ivorian Basin, GG = Gulf of Guinea, TSFC = Trou Sans Fond Canyon.

2 Setting of ODP Site 959

ODP Hole 959A is located in the eastern equatorial Atlantic Ocean ~120 km offshore Ivory Coast (latitude 3.627650, longitude -2.735200; Figure 1; Mascle et al., 1996). The site was drilled at 2102 m water depth on the southern edge of the Deep Ivorian Basin (DIB), just north of the top of the Côte d'Ivoire-Ghana Marginal Ridge (CIGMR). The CIGMR and DIB were formed due to the opening of the equatorial Atlantic during the Early Cretaceous (Basile et al., 1993). The relatively shallow bathymetric position on the slope of the marginal ridge allowed the recovery of relatively unaltered and undisturbed sediments.

Site 959 is suitable for studying monsoon dynamics as it is located in a region sensitive to seasonal shifts of the latitudinal position of the Intertropical Convergence Zone (ITCZ; Figure 2). During boreal summer (Figure 2a), the ITCZ is centered over the North African continent at ~18°N and southwest (SW) monsoons carry moisture from the tropical Atlantic into North Africa (Trauth et al., 2009). During boreal winter (Figure 2b), the ITCZ shifts southward to the Guinea coast and into the southern hemisphere African continent. In this period, surface airflow over North Africa is dominated by the northeast (NE) trade winds. A specific component of the NE trades, the Harmattan, transports dust from the Bodélé depression in Chad to the equatorial Atlantic (Prospero et al., 2002; Stuut et al., 2005; Trauth et al., 2009).

The Comoé River discharges into the Gulf of Guinea on the east side of Ivory Coast. However, sediment transport is effectively canalized by the Trou Sans Fond Canyon (TSFC), probably since the Oligocene, and therefore does not significantly influence Site 959 (Figure 1; Droz et al., 1985; Wagner, 1998). The main currents in the equatorial Atlantic are the westward flowing South Equatorial Current (SEC) and the eastward flowing Equatorial Undercurrent (EUC; Figures 2a & b; Norris, 1998a). The EUC carries cool, saline water from the South

Atlantic and is deflected northwards into the Gulf of Guinea, producing a strong thermocline (Norris, 1998a). The Guinea current flows eastward into the Gulf of Guinea and is reinforced by the North Equatorial Countercurrent (NECC) during boreal summer when the ITCZ moves northward (Figure 2a; Norris, 1998a). Prior to the establishment of the Guinea Current at ~5 Ma, it was hindered by a too southerly position of the Guinea coast (<2.5°N; Norris, 1998a), which was most likely also the case for the Early and Middle Miocene. In the eastern equatorial Atlantic, oceanic upwelling occurs along the Equatorial Divergence Zone (Wagner, 1998) and wind-induced coastal upwelling occurs off Ivory Coast and Ghana during boreal summer due to the combination of the Guinea Current and winds flowing parallel along the coast (Figure 2a; Norris, 1998a; Vallé et al., 2017; Wagner, 1998). A minor coastal upwelling event occurs during boreal winter due to the displacement of the ITCZ and corresponding wind systems (Wagner, 1998, 2002). Present-day sea surface temperatures (SSTs) in the Gulf of Guinea vary seasonally between ~25°C during the summer upwelling season, and ~29°C in winter (Djakouré et al., 2017).

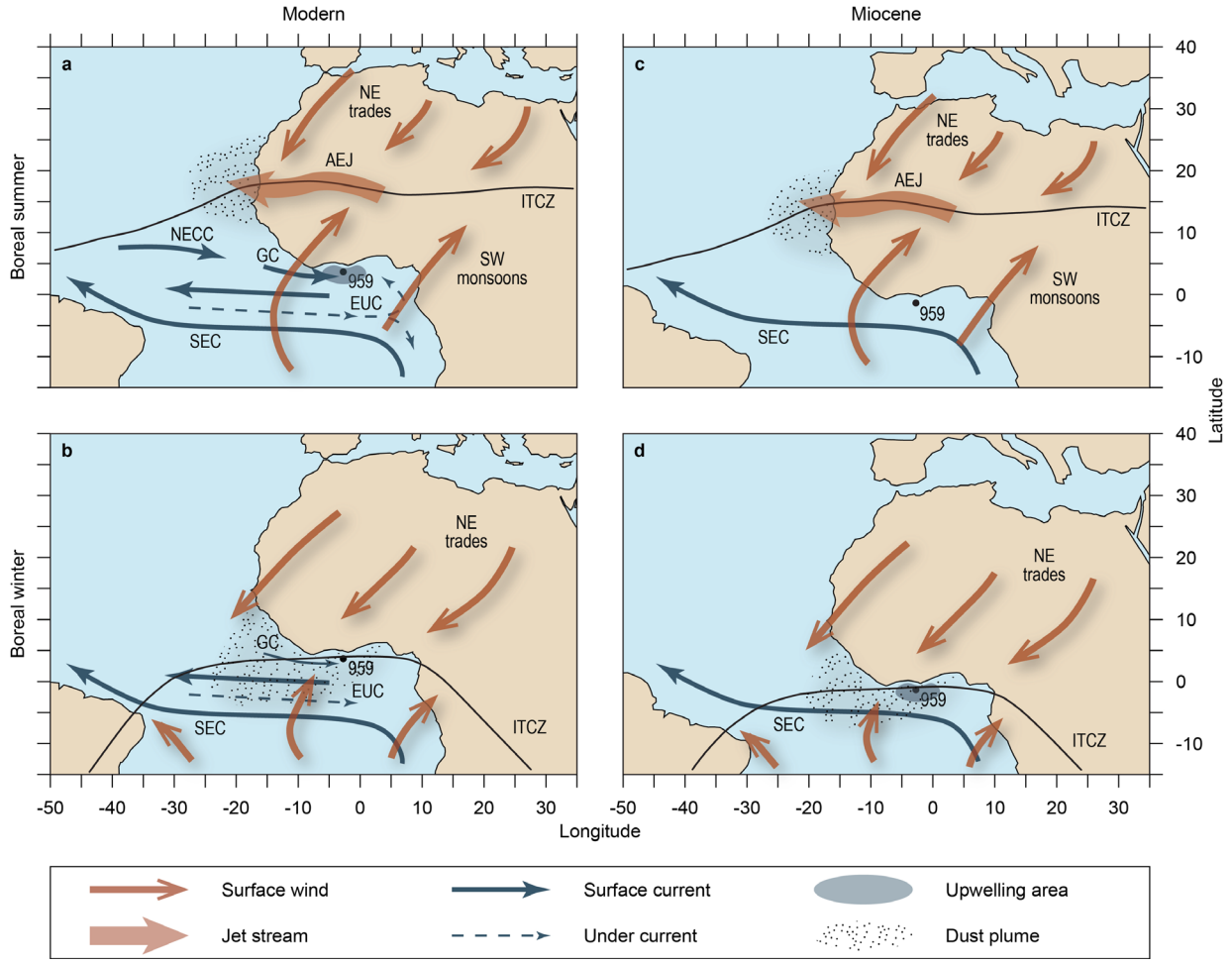

Figure 2. Maps with generalized atmospheric and oceanic circulation patterns around West Africa: modern situation for (**a**) boreal summer and (**b**) boreal winter (after Wang, 2009; Wagner, 1998; Norris, 1998a), and hypothesized Early to Middle Miocene situation for (**c**) boreal summer and (**d**) boreal winter. The continental boundaries are based on a 17 Ma

reconstruction using GPlates (Müller et al., 2018) with plate reconstructions of Seton et al. (2012) and paleomagnetic reference frame of Torsvik et al. (2012). At 17 Ma, Site 959 was located at a latitude of ~1°S +/- 2.5°. Abbreviations: NE = northeast, SW = southwest, AEJ = African Easterly Jet, ITCZ = Intertropical Convergence Zone, NECC = North Equatorial Countercurrent, GC = Guinea Current, SEC = South Equatorial Current, EUC = Equatorial Undercurrent.

3 Materials and Methods

3.1 Sediment properties

Lower to Middle Miocene sediments from ODP Hole 959A, cores 21X to 27X span 189 to 255 meters below sea floor (mbsf) and represent nannofossil chalks and clays with some organic matter, which are interbedded with diatomites in the lower part (cores 23X to 27X; 208 to 255 mbsf; Mascle et al., 1996; Wagner, 2002). Alternations in sediment color were observed from light to dark on 10 to 80 cm scale, in which siliceous phases generally represent the darker lithology and clay/calcareous phases represent the lighter lithology (Mascle et al., 1996).

3.2 Age model

Recently, a revised mbsf (rmbsf) depth scale was established by assuming 0.5 m gaps at core breaks (Wubben et al., 2023). Additionally, shipboard age control (Mascle et al., 1996; Norris, 1998b; Shafik et al., 1998) was updated with diatom and calcareous nannofossil biostratigraphy and chemostratigraphic markers (Figure 3; Wubben et al., 2023). These include the ~0.5‰ bulk $\delta^{18}O$ decrease at the onset of the MCO (16.9 Ma), the Monterey positive bulk $\delta^{13}C$ excursion, carbon-isotope maxima (CM) 1-4, and the MCO 'peak warming' event at 15.6 Ma (Figure 3; Wubben et al., 2023), which all have astronomically-tuned ages (Holbourn et al., 2007; Holbourn et al., 2015). Spectral analysis in the depth domain revealed main periodicities of ~12.5-10 m, ~3.5-2.5 m, ~1.5-1 m, and ~0.65-0.45 m, which were linked to ~400 kyr eccentricity, ~100 kyr eccentricity, obliquity (~41 kyr), and precession (~23-19 kyr), respectively (Wubben et al., 2023).

The bulk carbonate $\delta^{13}C$ record was chosen for astronomical tuning because of the clear expression of ~400 and ~100 kyr eccentricity (Wubben et al., 2023). Pronounced $\delta^{13}C$ minima were correlated to ~100 kyr eccentricity maxima (Figure 3), consistent with previous work (Holbourn et al., 2007; Liebrand et al., 2016; Pälike et al., 2006). Tuning of the interval after the onset of the MCO (17-15 Ma) was relatively straightforward and the resulting age model corresponds well with the bio- and chemostratigraphy (Figure 3). It was inferred that a ~100 kyr eccentricity maximum is missing between cores 22X and 23X (~227 rmbsf), resulting in a gap of ~60 kyr (Wubben et al., 2023). No significant amount of time is missing in the other core gaps.

Tuning of the pre-MCO interval (>17 Ma) was more complicated due to a discrepancy between diatom and calcareous nannofossil biostratigraphic tie-points (Wubben et al., 2023), and the short time span of high-resolution data relative to eccentricity cycles. Moreover, precession and obliquity are difficult to use for tuning due to uncertainties related to tidal dissipation and dynamical ellipticity (Zeebe & Lourens, 2022). Ultimately, the calcareous nannofossil tie-points were used because of their good constraints in the western equatorial Atlantic biostratigraphy, resulting in a hiatus of ~750 kyr between cores 25X and 26X (~258 rmbsf; Wubben et al., 2023). However, as these biostratigraphic tie-points could have an uncertainty, alternatives with a

smaller hiatus or continuous sedimentation cannot be excluded (Figure S7 of Wubben et al., 2023; Text S1; Figure S1). Extension of the high-resolution records towards the Oligocene might help to resolve the tuning of the pre-MCO interval. Despite this uncertainty in absolute age control, the clear recognition of ~100 kyr eccentricity-related $\delta^{13}C$ variations provides a confident relative age control for further cyclostratigraphic analyses.

Overall, the age model indicates that the studied interval (cores 21X-27X) covers 15.0-16.9 Ma and 17.7-18.2 Ma with average sedimentation rates of ~2.6 cm/kyr and ~3.7 cm/kyr, respectively. Spectral analysis in the time domain was mainly focused on periodicities of >100 kyr, while higher frequencies were not yet investigated in detail (Wubben et al., 2023).

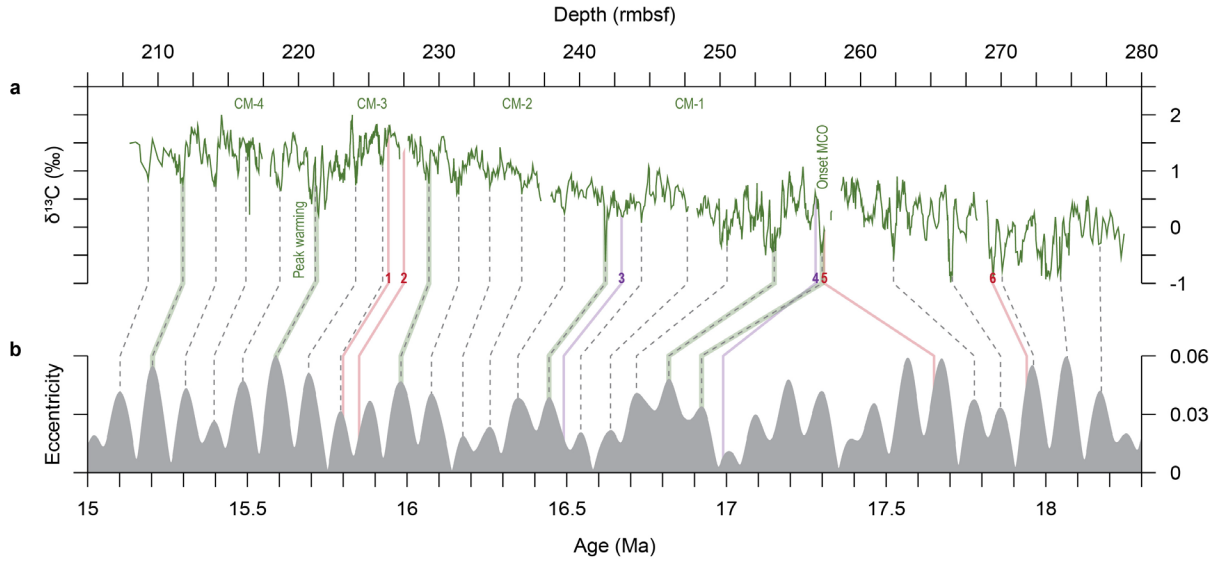

Figure 3. Astronomical tuning of the bulk carbonate $\delta^{13}C$ record. Tie-points (dashed gray lines; Wubben et al., 2023) connect pronounced minima in the $\delta^{13}C$ record in the depth domain (**a**) to eccentricity maxima in the La2004 eccentricity solution (**b**; Laskar et al., 2004). Positions and ages of nannofossil, diatom, and chemostratigraphic markers are indicated by the red, purple, and green lines, respectively (Wubben et al., 2023). Numbered biostratigraphic markers: 1 = top common D. *deflandrei*, 2 = bottom D. *signus*, 3 = top R. *marylandicus*, 4 = bottom A. *californicus* and C. *coscinodiscus*, 5 = bottom common S. *heteromorphus* (minimum depth), 6 = top S. *belemnos*.

3.3 Previously published proxy records

The sediment color, magnetic susceptibility (MS), bulk carbonate stable carbon and oxygen isotopic ratios ($\delta^{13}C$ and $\delta^{18}O$) and wt% $CaCO_3$ records of Wubben et al. (2023) have an average resolution of 1 cm (<1 kyr), 3 cm (1 kyr), 5 cm (2 kyr) and 15 cm (5 kyr), respectively (Figure 4). A record of the tetraether index of tetraethers with 86 carbon atoms (TEX_{86}; Schouten et al., 2002), which is positively correlated to SST, was generated by Wubben et al. (in press) at an average resolution of 13 cm (4 kyr). We also consider their record of the branched and isoprenoid tetraether (BIT) index (Hopmans et al., 2004) for soil-derived biomarker inputs. TEX_{86} values with a BIT index above 0.4 (n = 7) were removed as they are considered unreliable

(Weijers et al., 2006). See Wubben et al. (in press) for a detailed description of the biomarker data.

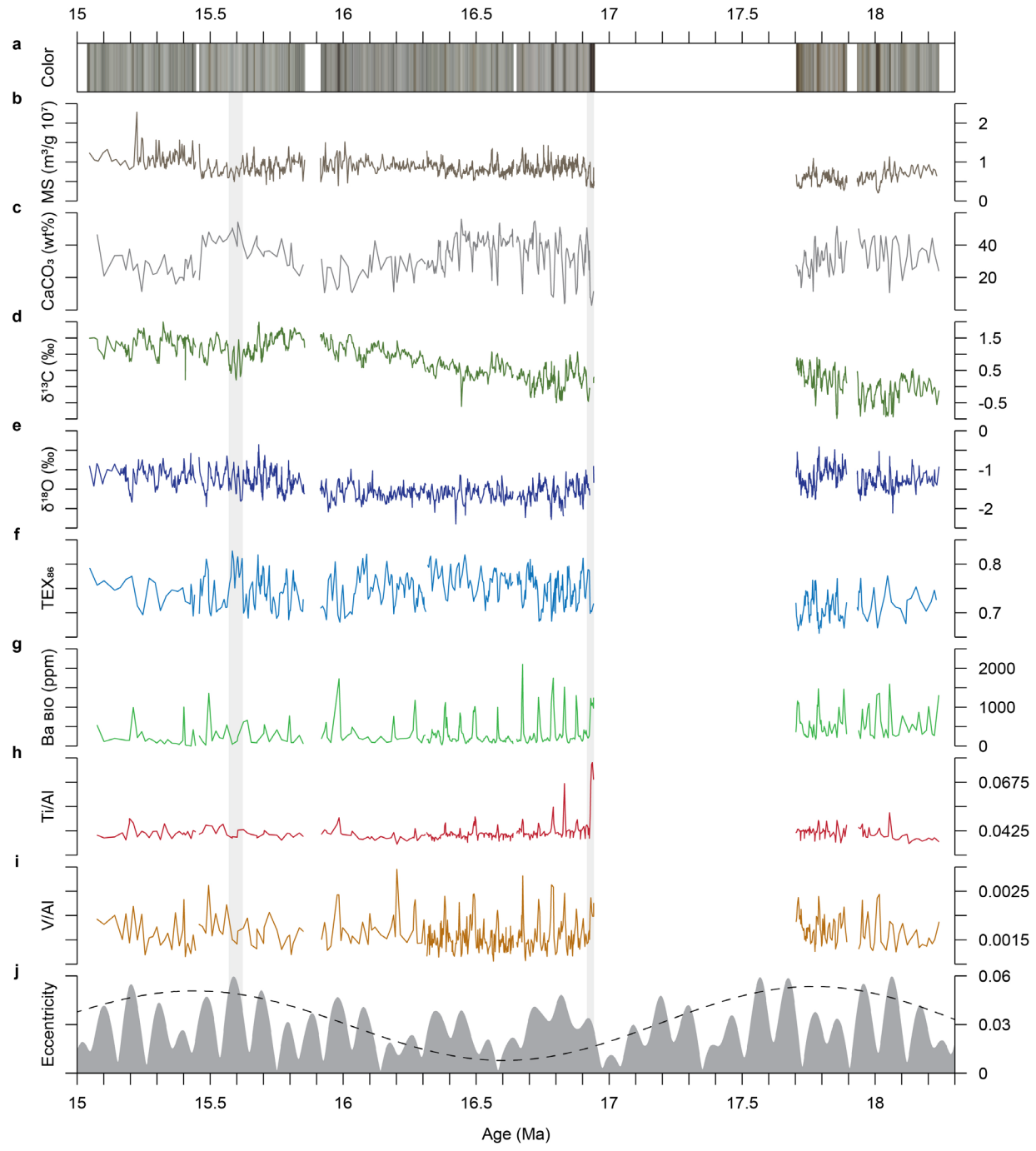

Figure 4. Overview of Early to Middle Miocene proxy data from Site 959: (**a**) color, (**b**) MS, (**c**) wt% $CaCO_3$, (**d**) $\delta^{13}C$, (**e**) $\delta^{18}O$, (**f**) TEX_{86}, (**g**) Ba_{bio}, (**h**) Ti/Al, (**i**) V/Al, and (**j**) the La2004 eccentricity solution (grey; Laskar et al., 2004) and its filtered 2.4 Myr eccentricity cycle (dashed

black). The gray bars represent the onset of the MCO at 16.9 Ma and the MCO 'peak warming' event at 15.6 Ma.

3.4 Bulk sediment elemental concentrations

Quantitative bulk elemental composition was measured with Inductively Coupled Plasma – Optical Emission Spectroscopy (ICP-OES) by Wubben et al. (2023) at an average resolution of 15 cm (5 kyr). The measured concentrations of Al, Ba, Ti and V (in ppm) were used to generate new geochemical records. Al was used as normalization parameter as it generally behaves conservatively (Calvert & Pedersen, 2007). The average recovery (accuracy) of Al, Ba, Ti and V was 99-106%, 91-102%, 100-106% and 83-101%, respectively. For all elements, the average analytical uncertainty based on duplicates was ~1-2% (deviation from the average divided by the average, times 100).

We used the concentration of biogenic Ba (Ba_{bio}) as a proxy for (export) productivity (Dymond et al., 1992; Kasten et al., 2001; Piela et al., 2012). At sites with significant terrestrial input, the barium signal in sediments may be strongly influenced by detrital barium present in aluminosilicates (Dymond et al., 1992). The Ba_{bio} signal was estimated by correcting the measured total Ba concentration for the detrital contribution (Dymond et al., 1992):

$$Ba_{bio} = Ba_{total} - \left(Al \times \left(\frac{Ba}{Al}\right)_{detrital}\right)$$

We determined a $(Ba/Al)_{detrital}$ value of 0.0029, as this resulted the lowest positive Ba_{bio} values (i.e., a value >0.0029 resulted in negative Ba_{bio} values). Although this value is lower than the 0.005-0.01 range based on the average crustal composition, it falls within the range of values obtained directly by sequential extraction for various sites in the Atlantic (0.0014-0.0041; Reitz et al., 2004).

The Ti/Al ratio was used as a proxy for aeolian (versus fluvial) input and sediment grain-size (Calvert & Pedersen, 2007; Govin et al., 2012; Martinez-Ruiz et al., 2015). Ti in aeolian dust mainly resides in heavy minerals, which are transported along with coarser quartz grains (Calvert & Pedersen, 2007; Martinez-Ruiz et al., 2015). Over the past 11 Myr at ODP Site 659, which is influenced by Saharan dust, the Al/Ti ratio closely agrees with the (Al+Fe)/(Si+K+Ti) proxy for fluvial versus aeolian input (Crocker et al., 2022), substantiating our approach. The V/Al ratio was used as a proxy for redox state. V is sensitive to minor changes in oxygen concentration and starts to accumulate as oxyhydroxides under dysoxic to suboxic conditions, in the absence of oxygen and sulfide (Calvert & Pedersen, 2007; Martinez-Ruiz et al., 2015).

3.5 Spectral analysis

The data was analyzed in the time domain using the astronomically-tuned age model presented by Wubben et al. (2023). Time series were sorted, interpolated to uniform spacing, and detrended to remove long-term trends using Acycle (Li et al., 2019). Depending on the time series, detrending was done linearly or using the locally weighted regression smoothing (LOWESS) method. Power spectra were generated with the multitaper method (time-bandwidth product = 2, pad factor = 5; Thomson, 1982) and first-order autoregressive (AR1) noise confidence levels (Meyers, 2012) using Astrochron (Meyers, 2014). Bandpass filtering was applied to isolate specific frequency components present in the time series using the Gauss algorithm in Acycle (Li et al., 2019).

For some intervals of the elemental (15.0-16.3 Ma and 17.9-18.2 Ma) and TEX_{86} data (15.0-15.4 Ma and 17.9-18.2 Ma), high-frequency analyses were not possible due to the relatively low resolution (~10-20 kyr). Bandpass filtering was only applied on scales that are appropriate for the resolution of the data. The color record, although providing valuable information on light-dark variations, was not used for spectral analyses as uneven lighting during shipboard core photography likely introduced artificial variability related to section and core length (Wubben et al., 2023).

4 Results

4.1 Elemental concentrations

Al concentrations are on average 6×10^4 ppm, varying between 2×10^4 ppm and 10×10^4 ppm (Figure S2). The Al record is very similar to the MS record in terms of trends and variability, with high Al corresponding to high MS (Figure S3e). Ba concentrations vary between 2×10^2 ppm and 23×10^2 ppm (Figure S2) and Ba_{bio} concentrations vary between 0 ppm and 21×10^2 ppm (Figure 4). Besides the difference in concentration, the Ba and Ba_{bio} records seem identical, implying that most of the Ba variability is related to Ba_{bio}. The Ba_{bio} record is characterized by pronounced peaks of $>8 \times 10^2$ ppm that occur regularly and generally correspond to darker sediment layers. Peaks are less well defined between 18.2-17.9 Ma and 16.3-15.0 Ma, possibly due to the lower sampling resolution. Ti concentrations vary between 1×10^3 ppm and 4×10^3 ppm (Figure S2) and Ti/Al ratios vary between 4×10^{-2} and 8×10^{-2} (Figure 4). The Ti record displays similar trends and variability as the Al record. Al-normalization results in a pattern with pronounced, regularly-occurring peaks between 16.9-16.3 Ma, similar to the Ba_{bio} record. The two largest Ti/Al peaks occur just after the onset of the MCO (16.9-16.8 Ma) with values of $>6 \times 10^{-2}$. The pre-MCO between 17.9-17.7 Ma displays smaller-scale variability and is characterized by a series of sharp minima. V concentrations vary between 5×10^1 ppm and 21×10^1 ppm (Figure S2) and V/Al ratios vary between 1×10^{-3} and 3×10^{-3} (Figure 4). The V record is relatively similar to the Al record, although V displays more pronounced peaks in the interval 16.9-16.3 Ma, which become even more pronounced after Al-normalization. For the Ba_{bio}, Ti/Al, and V/Al records, respectively, the standard deviation is ~113, ~24, and ~23 times larger than the deviation between duplicates (i.e., deviation from the average).

4.2 Astronomical variability in the proxy records

The Early to Middle Miocene proxy records of Site 959 show variability on scales of ~400 kyr, ~100 kyr, ~60-40 kyr, and ~27-17 kyr (Figures 4 & S4). Significant spectral power is found in these four frequency bands (Figure S4), consistent with the results of Wubben et al. (2023). Maxima of $\delta^{13}C$ generally correspond to maxima of $\delta^{18}O$, Ba_{bio}, Ti/Al, and V/Al, minima of wt% $CaCO_3$ and TEX_{86}, and darker sediment layers which are likely rich in biogenic silica (Figure 4). However, variability differs between proxy records and changes through time (Figure 5). Significant ~60-40 kyr variability following the onset of the MCO (16.9-16.3 Ma) deviates from the strong ~100 kyr pacing during the pre-MCO (18.2-17.7 Ma) and later part of the MCO (16.3-15.0 Ma). This transition to ~60-40 kyr variability concurs within a 2.4 Myr eccentricity minimum during which the amplitude of the ~100 kyr eccentricity cycle is reduced (Figure 4j). Because of the significant differences in variability in the proxy records and change in the eccentricity solution, the records are divided in three intervals: (1) 18.2-17.7 Ma, (2) 16.9-16.3 Ma, and (3) 16.3-15.0 Ma.

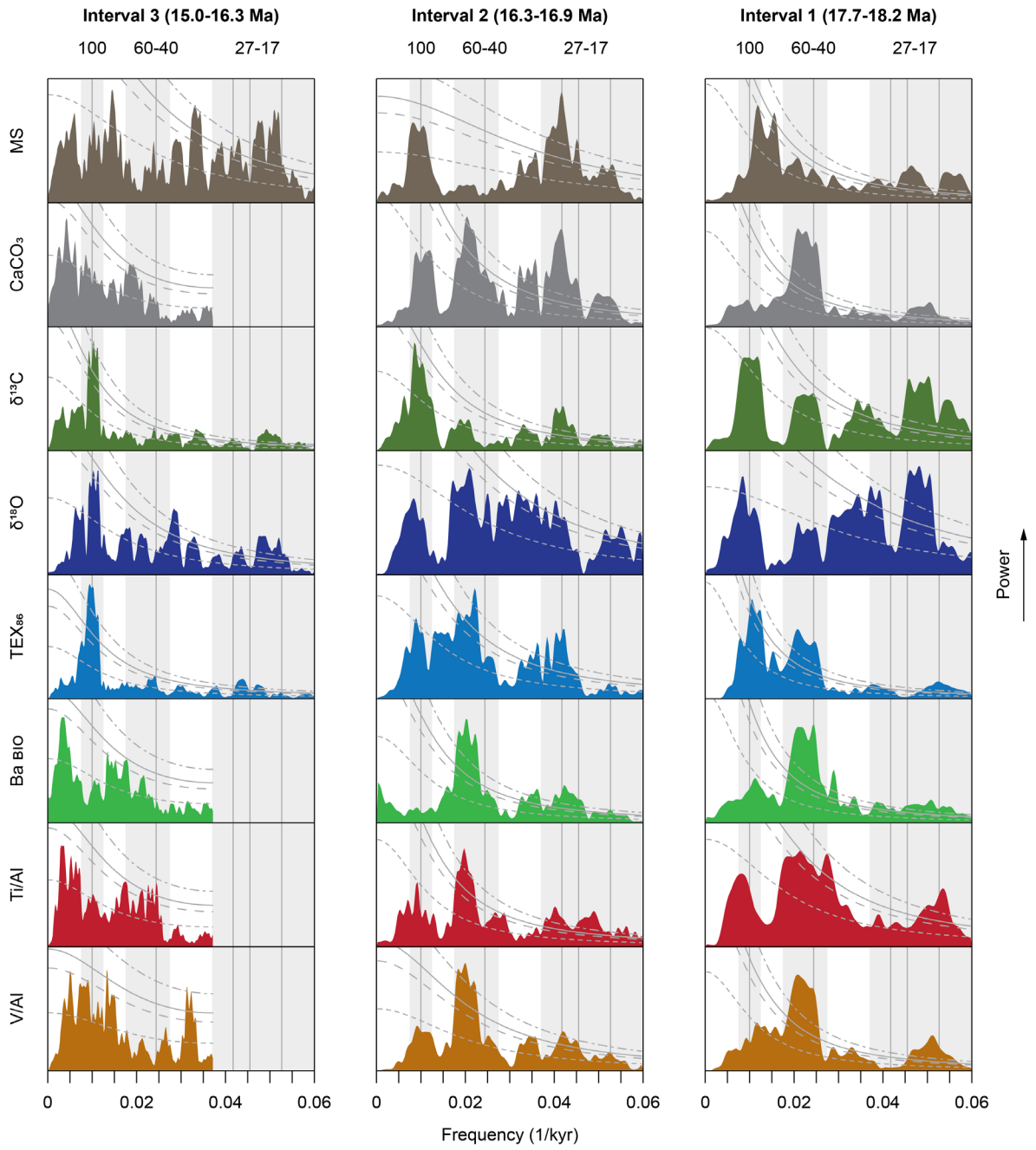

299

300 **Figure 5.** Power spectra of Site 959 proxy data for three intervals: 18.2-17.7 Ma, 16.9-16.3 Ma,
301 and 16.3-15.0 Ma. A linear scale is used for both the x (frequency) and y (power) axes. AR1 fit,
302 and 90%, 95%, and 99% confidence levels are indicated by the small dashed, large dashed, solid,
303 small-large dashed gray lines, respectively. The gray bars indicate important frequency bands

representing periodicities of ~100 kyr, ~60-40 kyr, and ~27-17 kyr. The vertical gray lines indicate exact periods of 100, 41, 24, 22, 19 kyr.

4.2.1 Interval 1 (18.2-17.7 Ma)

Before the onset of the MCO, the proxy records display strong variability on scales of ~100 kyr, ~60-40 kyr, and ~27-17 kyr (Figures 5 & 6). Records of $\delta^{13}C$, $\delta^{18}O$, TEX_{86} and MS display clear ~100 kyr cyclicity, but spectral power only reaches above the 95% confidence level for TEX_{86}. In the TEX_{86} record, ~100 kyr variability is asymmetrical between 17.9 and 17.7 Ma. This is characterized by a steep increase during high eccentricity followed by a gradual decrease with lower eccentricity, punctuated by smaller-scale fluctuations. The two rapid increases of TEX_{86} at ~17.86 and ~17.78 Ma concur with the two rapid and pronounced decreases of $\delta^{13}C$. Although ~100 kyr cyclicity is insignificant in records of wt% $CaCO_3$, Ba_{bio}, Ti/Al and V/Al, clear ~100 kyr variability can be recognized in the Ba_{bio} and V/Al records between 17.9 and 17.7 Ma.

~60-40 kyr cyclicity dominates records of wt% $CaCO_3$, Ba_{bio}, Ti/Al and V/Al, but it is also significantly present in $\delta^{13}C$ and TEX_{86}. A change in dominant pacing is observed in the Ba_{bio} and sediment color records, from ~60-40 kyr between 18.2 and 17.9 Ma to ~100 kyr between 17.9 and 17.7 Ma.

Significant spectral power in the ~27-17 kyr band is present in all proxy records. However, between 18.2 and 17.9 Ma, the resolution of the elemental and TEX_{86} records is insufficient to record variations on this scale. Bandpass filtering reveals that greater amplitudes of the ~27-17 kyr cycle roughly correspond to eccentricity maxima, most clearly visible in records of $\delta^{13}C$ and $\delta^{18}O$ (Figure 6).

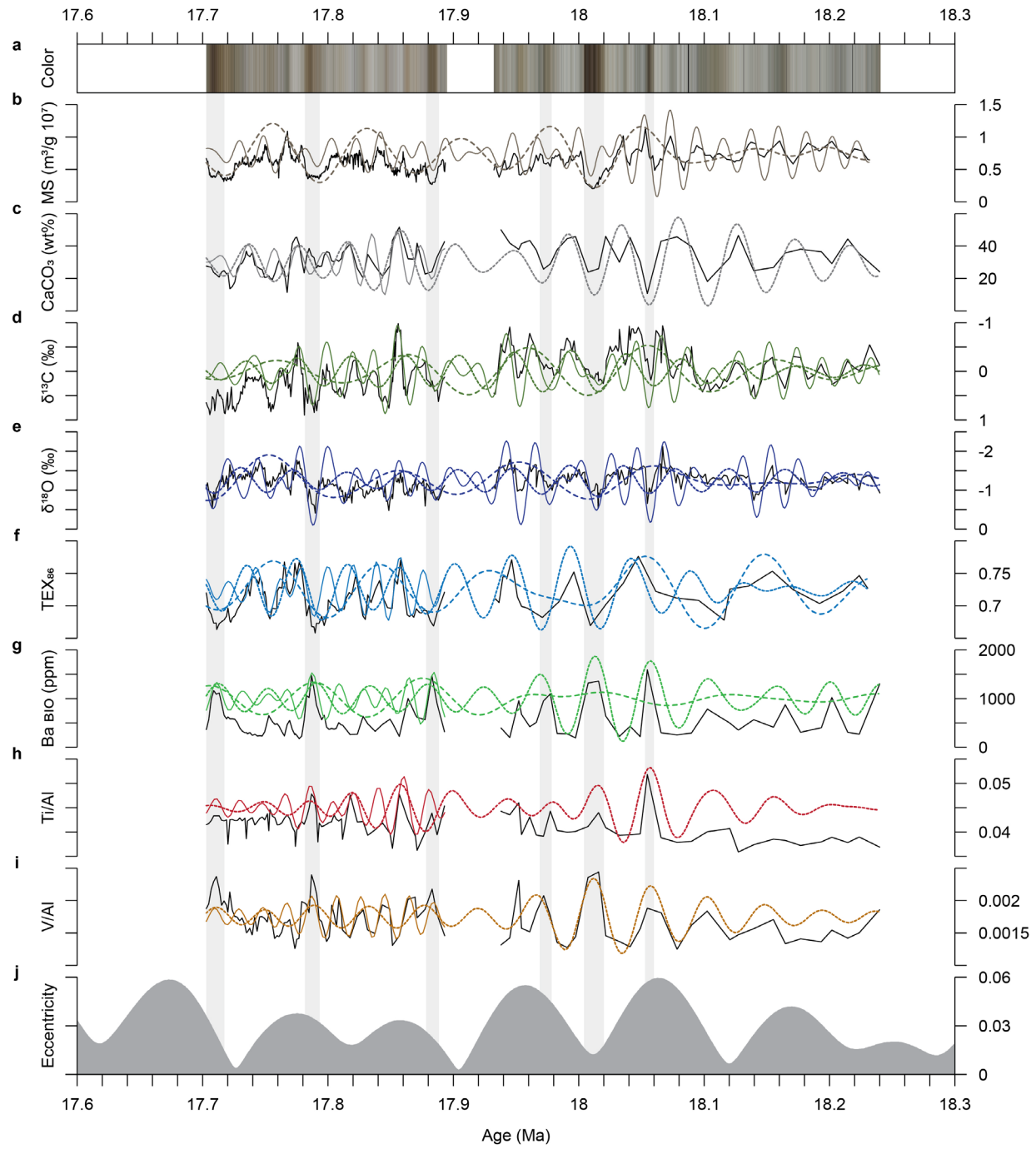

Figure 6. Interval 1 (18.2-17.7 Ma) with Site 959 proxy data and bandpass filters: (**a**) color, (**b**) MS, (**c**) $CaCO_3$, (**d**) $\delta^{13}C$, (**e**) $\delta^{18}O$, (**f**) TEX_{86}, (**g**) Ba_{bio}, (**h**) Ti/Al, (**i**) V/Al, and (**j**) the La2004 eccentricity solution (Laskar et al., 2004). The gray bars indicate relatively dark sediment layers that correspond to peaks of Ba_{bio}. Bandpass filters of ~100 kyr, ~60-40 kyr, and ~27-17 kyr cyclicity are represented by dashed, dotted, and solid colored lines, respectively. The following bandpass filter widths (in 1/kyr) were used: 0.0086-0.017 and 0.036-0.061 for MS, 0.006-0.014, 0.018-0.027 and 0.03-0.061 for $\delta^{13}C$, 0.0055-0.014, 0.019-0.0265 and 0.03-0.058 for $\delta^{18}O$, 0.017-0.028 and 0.036-0.06 for $CaCO_3$, 0.007-0.014, 0.0175-0.028 and 0.035-0.06 for TEX_{86},

0.007-0.014, 0.017-0.0275 and 0.036-0.06 for Ba_{bio}, 0.016-0.03, 0.036-0.06 for Ti/Al, and 0.017-0.027 and 0.04-0.06 for V/Al.

4.2.2 Interval 2 (16.9-16.3 Ma)

The $\delta^{13}C$ record displays clear ~100 kyr cyclicity (Figure 7), which almost reaches above the 95% confidence level (Figure 5). Relatively weak power around this period is found in records of $\delta^{18}O$, wt% $CaCO_3$, MS, TEX_{86}, Ti/Al, and V/Al. For TEX_{86}, two clear ~100 kyr cycles can be recognized between ~16.5 and ~16.3 Ma (in the upper part of this interval). The Ba_{bio} record displays no peak in spectral power around a period of ~100 kyr.

The records of wt% $CaCO_3$, TEX_{86}, Ba_{bio}, Ti/Al, V/Al, and sediment color are characterized by significant ~60-50 kyr variability, which is absent in records of $\delta^{13}C$, $\delta^{18}O$, and MS (Figures 5 & 7). Bandpass filters centered at ~60-50 kyr follow the pronounced peaks of Ba_{bio}, Ti/Al, and V/Al, minima of wt%$CaCO_3$ and TEX_{86}, and darker sediment layers. The ~60-50 kyr TEX_{86} cycle around ~16.76 Ma has an asymmetric shape. All proxy records display significant spectral power in the ~27-17 kyr periodicity band. Bandpass filtering reveals that two or three ~27-17 kyr cycles are present within one ~60-50 kyr cycle.

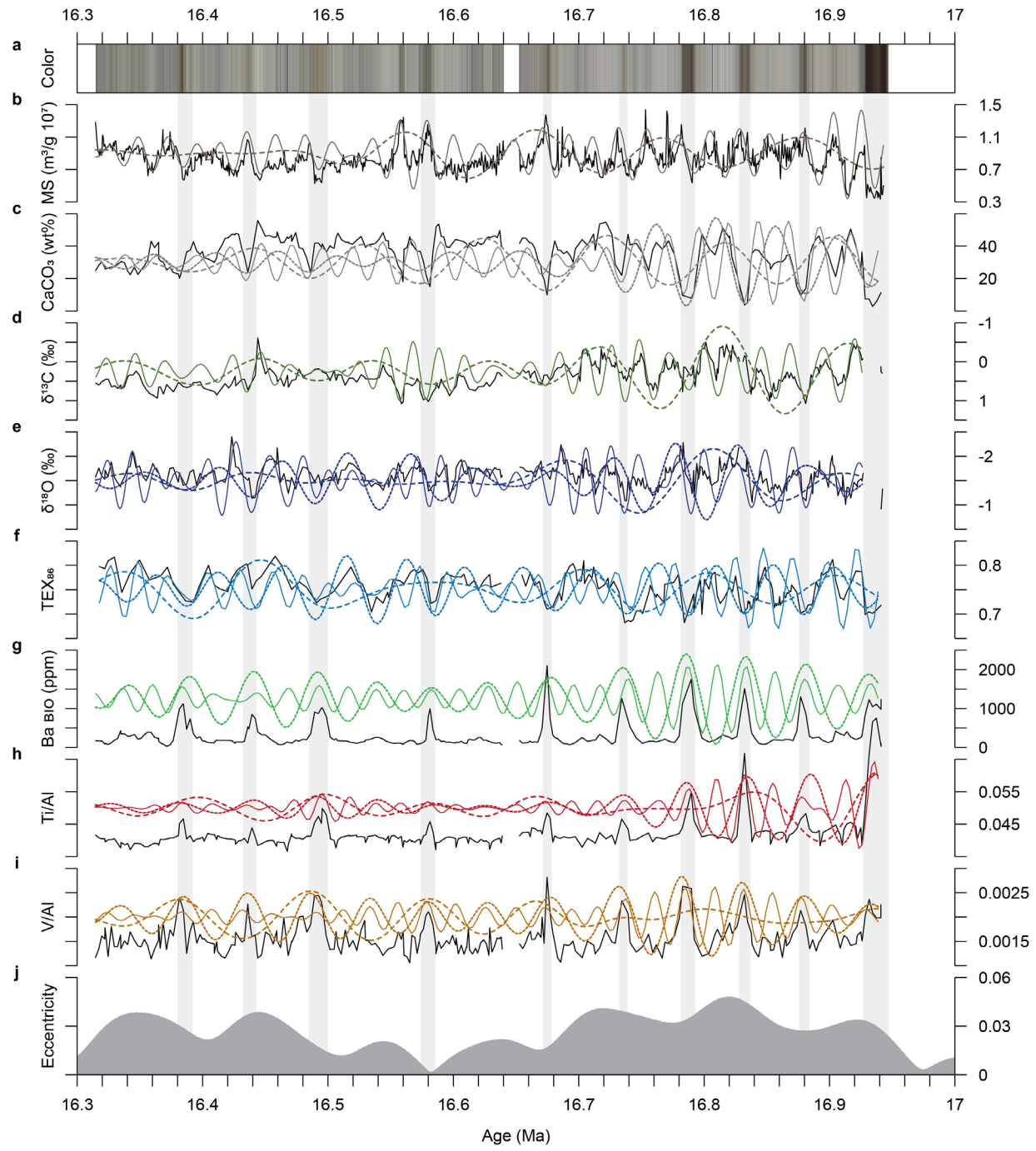

Figure 7. Interval 2 (16.9-16.3 Ma) with Site 959 proxy data and bandpass filters: (**a**) color, (**b**) MS, (**c**) $CaCO_3$, (**d**) $\delta^{13}C$, (**e**) $\delta^{18}O$, (**f**) TEX_{86}, (**g**) Ba_{bio}, (**h**) Ti/Al, (**i**) V/Al, and (**j**) the La2004 eccentricity solution (Laskar et al., 2004). The gray bars indicate relatively dark sediment layers that correspond to peaks of Ba_{bio}. Bandpass filters of ~100 kyr, ~60-40 kyr, and ~27-17 kyr cyclicity are represented by dashed, dotted, and solid colored lines, respectively. The following bandpass filter widths (in 1/kyr) were used: 0.006-0.013 and 0.037-0.055 for MS, 0.007-0.0135 and 0.037-0.055 for $\delta^{13}C$, 0.005-0.012, 0.0155-0.0235 and 0.037-0.0577 for $\delta^{18}O$, 0.007-0.014, 0.0165-0.024 and 0.037-0.047 for $CaCO_3$, 0.006-0.012, 0.017-0.024 and 0.037-0.055 for TEX_{86},

0.0165-0.024 and 0.038-0.048 for Ba_{bio}, 0.006-0.014, 0.0165-0.024 and 0.037-0.0515 for Ti/Al, and 0.006-0.014, 0.0165-0.024 and 0.038-0.048 for V/Al.

4.2.3 Interval 3 (16.3-15.0 Ma)

After 16.3 Ma, the high-resolution proxy records are dominated by ~100 kyr and ~27-17 kyr variability (Figures 5 & 8). Significant ~100 kyr cyclicity is present in records of $\delta^{13}C$, $\delta^{18}O$, and TEX_{86}. The amplitude of the ~100 kyr cycle in TEX_{86} follows the orbital solution of eccentricity, with greater amplitudes corresponding to ~400 kyr eccentricity maxima. Additionally, the TEX_{86} record shows significant ~41 kyr cyclicity, which follows relatively pronounced TEX_{86} minima, and greater amplitudes occur during ~400 kyr eccentricity minima.

For MS and the elemental data, spectral peaks around a period of 100 kyr are insignificant (below or around the AR1 fit level). However, for Ti/Al, this filtered cyclicity does approximately follow orbital eccentricity. The elemental data show somewhat higher, although still insignificant (below the 90% confidence level), peaks at periods of ~150-300 kyr. This could be an artifact related to the low resolution, or a real signal as weak spectral power (below the AR1 fit level) in this period range is also present in the MS data.

All high-resolution records (i.e., $\delta^{13}C$, $\delta^{18}O$, TEX_{86}, and MS) display significant ~27-17 kyr cyclicity. For $\delta^{13}C$ and $\delta^{18}O$, greater amplitudes of the ~27-17 kyr cycle generally correspond with ~100 kyr eccentricity maxima, particularly during the 15.6 Ma ‘peak warming’ event. This event corresponds to an interval with a relatively light sediment color and shows relatively high TEX_{86} values.

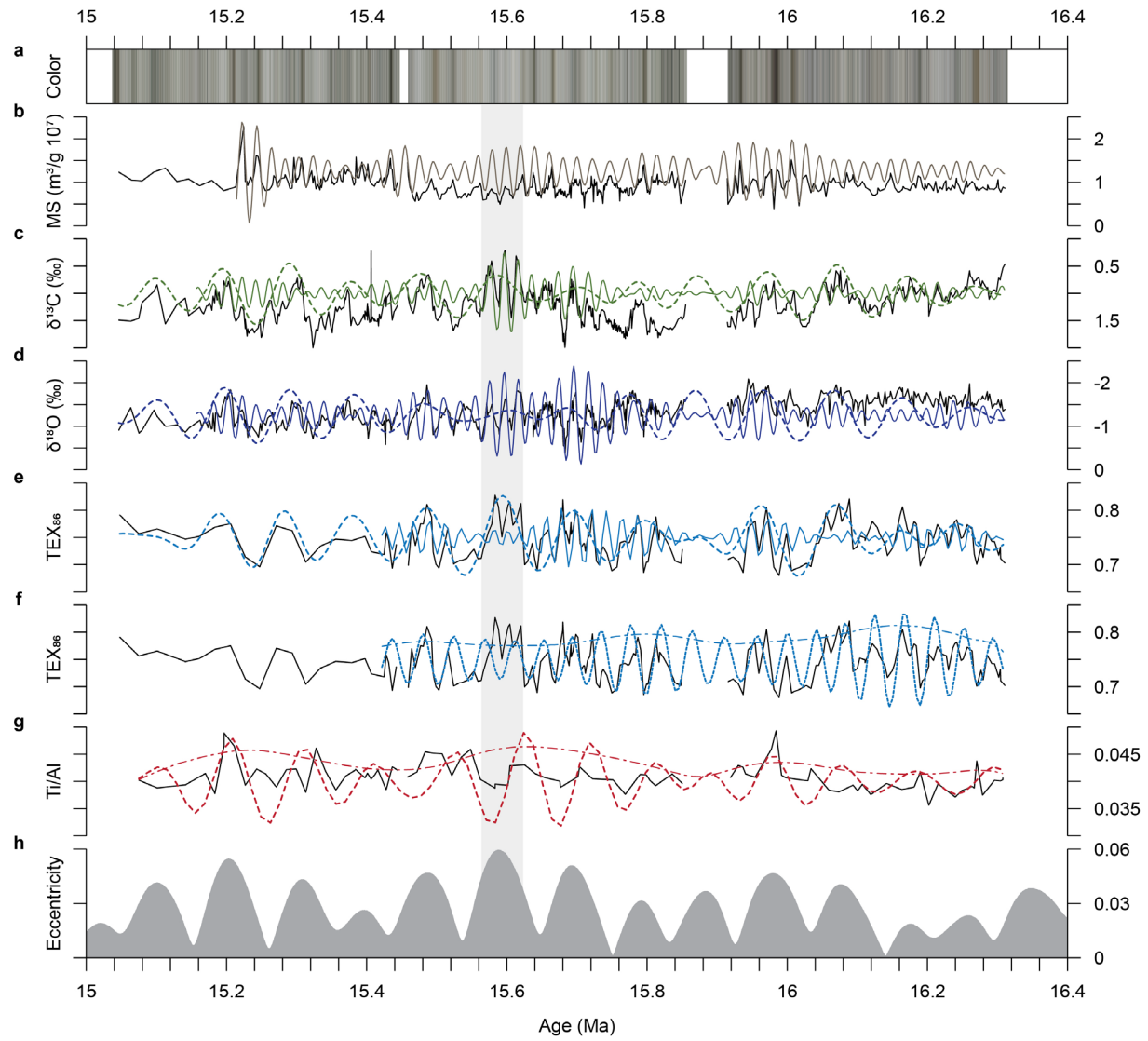

Figure 8. Interval 3 (16.3-15.0 Ma) with Site 959 proxy data and bandpass filters: (**a**) color, (**b**) MS, (**c**) $\delta^{13}C$, (**d**) $\delta^{18}O$, (**e-f**) TEX_{86}, (**g**) Ti/Al, and (**h**) the La2004 eccentricity solution (Laskar et al., 2004). The gray bar indicates the MCO 'peak warming' event at 15.6 Ma. Bandpass filters of ~100 kyr, ~60-40 kyr, and ~27-17 kyr cyclicity are represented by dashed, dotted, and solid colored lines, respectively. Amplitude modulations are represented by the dashed-dotted colored lines. The following bandpass filter widths (in 1/kyr) were used: 0.0405-0.058 for MS, 0.007-0.0135 and 0.039-0.059 for $\delta^{13}C$, 0.0085-0.0125 and 0.0405-0.0555 for $\delta^{18}O$, 0.006-0.013, 0.021-0.026 and 0.04-0.055 for TEX_{86}, and 0.008-0.0122 for Ti/Al.

5 Discussion

The Early to Middle Miocene proxy records of Site 959 reveal periodicities of ~400 and ~100 kyr, ~41 kyr, and ~27-17 kyr, which are likely related to ~400 and ~100 kyr eccentricity, obliquity, and precession, respectively, and additionally ~60-50 kyr cyclicity. Fluctuations of TEX_{86} reflect temperature variations of the shallow subsurface and were interpreted to represent

variations in upwelling intensity, consistent with dinoflagellate cyst analyses (Wubben et al., in press). As upwelling boosts productivity, this is in agreement with the occurrence of productivity (Ba_{bio}) peaks during SST (TEX_{86}) minima. Concurring V/Al peaks suggest reduced oxygen conditions, possibly due to increased decomposition of organic matter. Peaks of Ti/Al are interpreted as periods of increased dust supply and occurred when upwelling was intensified. Terrestrial input was mainly aeolian, as Site 959 was not strongly affected by fluvial processes during the Early to Middle Miocene (Wubben et al., in press). These cyclic variations in upwelling intensity and dust supply point to changes in atmospheric and hydrologic circulation related to the presence of a monsoon system. To further understand this astronomically-forced system, we first discuss the origin of ~60-50 kyr cyclicity which is present is many of the proxy records. Subsequently, by looking at variability at scales of precession, obliquity, and eccentricity, we discuss how Site 959 was affected by monsoon dynamics, subdivided in a dust and SST aspect, and evaluate potential high-latitude influence.

5.1 Origin of 60-50 kyr cyclicity

Significant ~60-50 kyr cyclicity is found just after the onset of the MCO (16.9-16.3 Ma) in records of wt% $CaCO_3$, TEX_{86}, Ba_{bio}, Ti/Al, and V/Al. The bulk $\delta^{13}C$ record, however, remains dominated by eccentricity and precession in this interval, indicating that it was decoupled. Significant power around ~60-50 kyr is also present before the onset of the MCO (18.2-17.7 Ma). However, the pre-MCO age model has uncertainties and a shift might transfer this power towards the 41 kyr band. Interestingly, in the subtropical Atlantic between 1 and 2 Ma, strong ~54 kyr cyclicity is also found in the dust record, while benthic $\delta^{18}O$ remains dominated by 41 kyr obliquity (Tiedemann et al., 1994). Intermittent ~50 kyr cyclicity has also been found in the Late Oligocene to Early Miocene $\delta^{18}O$ record from the Pacific (Beddow et al., 2018). This was suggested to be related to an offset obliquity cycle or a harmonic of the ~100 kyr eccentricity cycle (Beddow et al., 2018).

A ~54 kyr component is actually present in the astronomical solution of obliquity (e.g., Hinnov, 2013), but it is small compared to the 41 kyr component and therefore cannot produce significant ~54 kyr variability in the proxy records. No clear correlation is found between ~100 kyr and ~60-50 kyr cyclicity (Figures 7 & 9), indicating that the latter was not a harmonic of ~100 kyr eccentricity. The ~60-50 kyr cyclicity also does not seem to be a result of the eccentricity-based age model, as tuning to precession still produces spectral power in this period as well as at 41 kyr (Figures S5, S6 & S7; Table S1).

It seems that ~60-50 kyr cyclicity originates from ~27-17 kyr variability that is amplified every second or third cycle, similar to interference patterns between precession and obliquity in the astronomical solution. Indeed, the amplitude modulation of the standardized tilt and precession (TP) curve corresponds very well with ~60-50 kyr cyclicity in the proxy records (Figure 9). This amplitude modulation cycle is dominated by power around ~60-50 kyr (Figure S8), which consists of combination tones of ~22-24 kyr precession and obliquity (frequency precession minus frequency obliquity; von Dobeneck & Schmieder, 1999). Additional power is present around ~35 kyr due to the combination tone of ~19 kyr precession and obliquity, which might explain the observed ~35 cyclicity in the $\delta^{18}O$ and MS records during the MCO (Figure 5; Wubben et al., 2023). Power at ~35 kyr is weaker during 2.4 Myr eccentricity minima (e.g., just after the MCO onset), because the ~19 kyr precession component is weaker. Therefore, we

suggest that the observed ~60-50 kyr cyclicity is most likely related to combination tones of precession and obliquity.

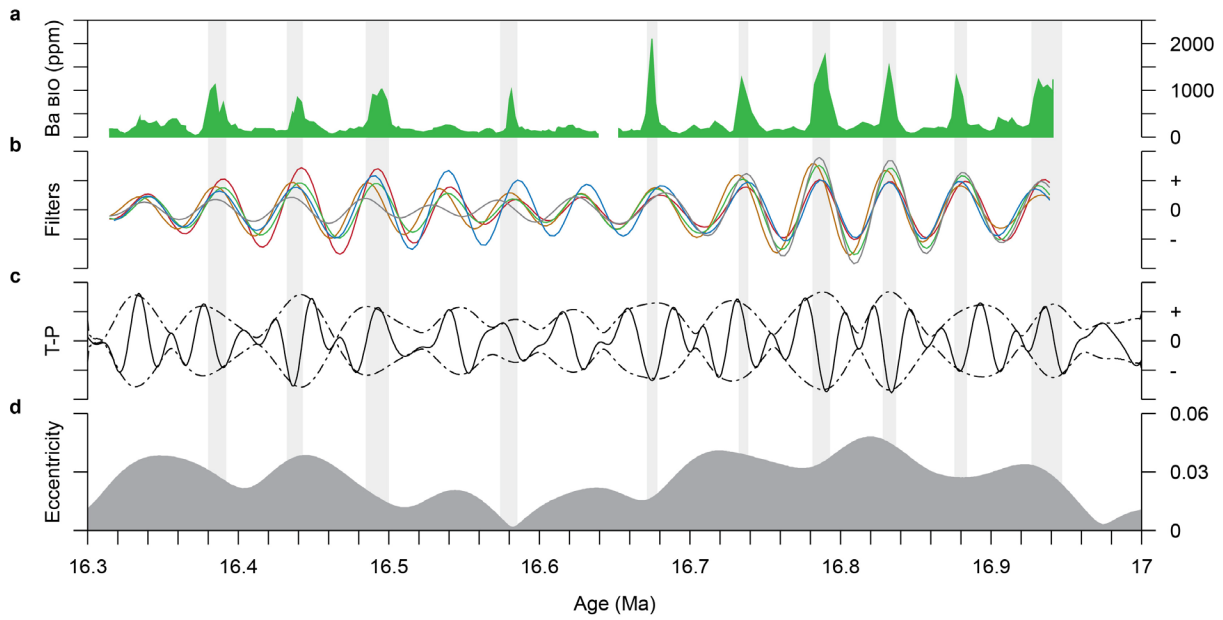

Figure 9. 60-50 kyr cyclicity in Site 959 proxy records just after the MCO onset (16.9-16.3 Ma). The Ba_{bio} record (**a**) is compared to ~60-50 kyr bandpass filters of $CaCO_3$ (gray), TEX_{86} (blue), Ba_{bio} (green), Ti/Al (red), and V/Al (orange; **b**), the standardized tilt and reversed-precession (T-P) curve (solid black) with its amplitude modulation (dashed-dotted black; **c**), and eccentricity (**d**) of the La2004 solution (Laskar et al., 2004). The gray bars indicate relatively dark sediment layers that correspond to peaks of Ba_{bio}. See caption of Figure 7 for bandpass filter widths.

5.2 Dust supply

5.2.1 Precession and obliquity phasing

At present, a large dust source is located in North Africa (Prospero et al., 2002) and NE trade winds transport dust from central North Africa to the eastern equatorial Atlantic during winter (Figure 2b; Prospero et al., 2002; Stuut et al., 2005). Aridification of North Africa occurred from the Early Miocene, during which the climate was mainly semiarid with restricted arid areas (Hounslow et al., 2017; Z. Zhang et al., 2014). Modelling studies, using relatively recent (<1 Ma) boundary conditions, show that decreased boreal summer insolation during precession maxima and obliquity minima resulted in decreased moisture transport from the tropical Atlantic towards North Africa and decreased continental precipitation in that region (Bosmans, Drijfhout, et al., 2015). This decreases vegetation cover and increases aridity, which together with wind strength/direction determines dust supply to the ocean (Trauth et al., 2009).

Just after the onset of the MCO (16.9-16.3 Ma), the Ti/Al record is strongly influenced by precession and obliquity, expressed as their combination tones. Precession-induced variations of Ti/Al also occurred in the eastern Mediterranean over at least the last 10 Myr, during which high values were linked to periods of increased aeolian versus fluvial input during precession maxima (Konijnendijk et al., 2014; Larrasoaña et al., 2003; Lourens et al., 2001; Schenau et al., 1999).

Similarly, off Northwest Africa for the past 11 Myr, dust flux maxima were linked to increased South Saharan and Sahelian aridity during precession maxima (Crocker et al., 2022; Tiedemann et al., 1994). Although the influence of obliquity on low-latitude insolation is small, it does affect low-latitude interhemispheric insolation gradients and therefore African monsoon dynamics (Bosmans, Drijfhout, et al., 2015; Bosmans, Hilgen, et al., 2015). Obliquity signals have been recorded in dust records from the eastern Mediterranean and off Northwest Africa covering the last 3 to 11 Myr, with dust maxima linked to obliquity minima (Crocker et al., 2022; Konijnendijk et al., 2014; Larrasoaña et al., 2003; Lourens et al., 2001; Tiedemann et al., 1994).

An opposite phase relationship has been assumed for Fe intensity maxima at Site 959 between 2 and 6 Ma, which generally correspond to Ti intensity and Ti/Al maxima (Figure S9; Vallé et al., 2017). Fe intensity maxima were linked to precession minima and obliquity maxima (i.e., boreal summer insolation maxima; Vallé et al., 2017). This precession phasing might be possible if dust would have originated from southern Africa, which was the case for the Cretaceous when the African continent was displaced to the south compared to the present and Miocene (Beckmann et al., 2005). However, only small dust sources are currently located in southern Africa (Prospero et al., 2002) and the Miocene continental configuration was more similar to the present than to the Cretaceous. Moreover, their age model resulted in errors up to 50 kyr for the 3.5-2.8 Ma interval, possibly due to incorrectly assumed phase relationships, and a revised age model for this interval indicates that Fe intensity maxima were related to obliquity minima (Figure S10; van der Weijst et al., 2020). Therefore, we assume that dust (Ti/Al) maxima during the Early to Middle Miocene at Site 959 were related to precession maxima and obliquity minima (i.e., boreal summer insolation minima).

5.2.2 Eccentricity

Eccentricity is the amplitude modulator of precession and power at its frequency bands, which is basically absent in the insolation forcing, can be produced by a non-linear response to precession forcing. A significant expression of eccentricity has been found in dust records from the eastern Mediterranean, off Northwest Africa, and in the eastern equatorial Atlantic over the last 6 Myr (Larrasoaña et al., 2003; Tiedemann et al., 1994; Vallé et al., 2017). However, no significant ~100 kyr signal is present in the Early to Middle Miocene Ti/Al record (Figure 5) and its phasing relative to eccentricity is not consistent (Figure 10). Dust maxima roughly correspond to eccentricity minima between 16.7-16.3 Ma, while they mostly correspond to eccentricity maxima between 16.3-15.0 Ma. Higher amplitudes of the ~100 kyr signal approximately occur during ~400 kyr eccentricity maxima (Figure 10).

Dust maxima corresponded to eccentricity maxima in dust records off Northwest Africa between 3 and 5 Ma (Tiedemann et al., 1994) and from Site 959 between 2 and 6 Ma (Vallé et al., 2017). The dust flux was mainly dependent on low-latitude insolation forcing prior to 3 Ma, while the response was more complex after 3 Ma due to the influence of the northern hemisphere glaciations (Tiedemann et al., 1994). For the last 0.5 Myr, dust maxima off West and East Africa occurred during major ~100 kyr-driven glacials (deMenocal, 2004). Therefore, an antiphase relationship might indicate an influence of glaciations, while an in-phase relationship suggests mainly low-latitude forcing. However, these dust signals were based on the terrigenous fraction, which could be biased by glacial-interglacial carbonate dissolution (Skonieczny et al., 2019).

A relatively weak ~100 kyr but strong ~400 kyr expression has been found in the eastern Mediterranean hematite-based dust record for the last 3 Myr, with dust maxima corresponding to

~400 kyr eccentricity minima (Larrasoaña et al., 2003). Trauth et al. (2009) proposed that the contrasting eccentricity phasing originated from differences in dust transportation mechanisms. However, the hematite record shows a significant increase around 2.5 Ma which is not observed for Ti/Al at the same site (Larrasoaña et al., 2003; Lourens et al., 2001), indicating that the response might also depend on the type of dust proxy. Our MS record also differs from Ti/Al, as Ti/Al peaks can corresponds to maximum or minimum MS values, possibly due to dilution effects (Wubben et al., 2023). This shows that there can be several factors that complicate the dust response to eccentricity. In addition, the signal might not be clearly recorded between 16.9 and 16.3 Ma due to the reduced power of the ~100 kyr eccentricity cycle during a 2.4 Myr eccentricity minimum (Figure 4j), and might be obscured between 16.3 and 15.0 Ma due to the low resolution.

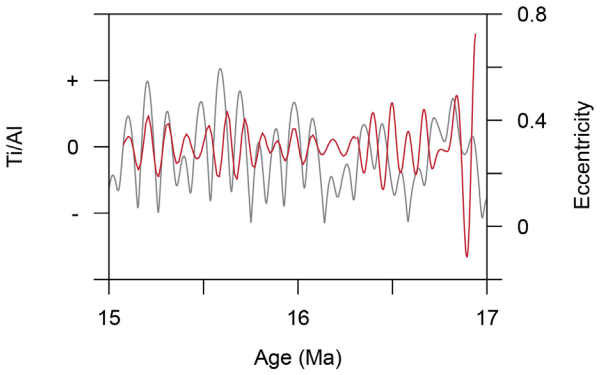

Figure 10. Bandpass filters of ~100 kyr cyclicity in the Ti/Al record (red) compared to the La2004 eccentricity solution (gray; Laskar et al., 2004) for the MCO interval (17-15 Ma). See caption of Figures 7 and 8 for bandpass filter widths.

5.3 Sea surface temperature

5.3.1 Seasonal and precession phasing of upwelling

The present-day main upwelling event in the Gulf of Guinea occurs during boreal summer. However, a more southerly position of the Guinea coast likely prevented the inflow of the NECC and EUC, the establishment of the Guinea Current, and thus the establishment of coastal upwelling during boreal summer (Figure 2c; Norris, 1998a; Wagner, 2002). In this scenario, the westward flowing SEC would be the main current in the Gulf of Guinea. Therefore, it was proposed that coastal upwelling more likely occurred during boreal winter in response to the southward displacement of the ITCZ and westward blowing surface winds, displacing surface waters to the left in the southern hemisphere (Figure 2d; Wagner, 2002). This suggests that more intense or prolonged upwelling and therefore lowest SSTs occurred during precession maxima (i.e., boreal summer insolation minima and austral summer insolation maxima), in response to a more/prolonged southerly position of the ITCZ (Norris, 1998a). However, considering a more southern position of Africa, it might also be possible that the Gulf of Guinea was significantly affected by the Atlantic cold tongue, which forms during early boreal summer as southeast (SE) trade winds intensify (Caniaux et al., 2011). For the last 250 kyr, it has been inferred that increased equatorial upwelling and coolest eastern equatorial SSTs occurred during precession maxima, because the SE trade winds intensify as the West African monsoon weakens

(McIntyre et al., 1989). This suggests that lowest SSTs most likely occurred during precession maxima, either due to intensified coastal or equatorial upwelling. This is in agreement with the expected precession phasing of dust input (Ti/Al).

Comparison to simulations of Atlantic SST is complicated, because they do not always incorporate differences in precession or continental configuration. As expected, a westward flowing current dominates in the Gulf of Guinea when the Guinea coast is located just above the equator like in the Eocene simulation (Acosta et al., 2022). However, the simulations of Acosta et al. (2022) do not show significant coastal upwelling in the Gulf of Guinea in any of the Cenozoic simulations, including the preindustrial, suggesting that the model does not capture this process. In these simulations, lowest eastern equatorial SSTs occurred during boreal summer throughout the Cenozoic, which seems to be related to the Atlantic cold tongue. Bosmans, Drijfhout, et al. (2015) performed simulations with different astronomical parameters, but with a modern continental configuration, for which the SST outputs are included in our Supporting Information (Figure S11). These show lower SSTs along the Guinea coast during precession minima throughout the year, possibly related to intensified coastal upwelling under the modern land-sea distribution. Around the equator, SSTs are lower during precession minima for boreal winter and spring, but higher during precession minima for boreal autumn. The latter is in agreement with intensified equatorial upwelling during precession maxima (although with a different seasonal timing as expected).

5.3.2 Non-linear response

SST variability at Site 959 was strongly paced by ~100 kyr eccentricity prior to the MCO (17.9-17.7 Ma) and during the MCO between 16.5-15.0 Ma. The ~100 kyr signal is weak between 16.9-16.5 Ma, which is in agreement with the occurrence of a node in eccentricity (2.4 Myr minimum) during which the amplitude of the ~100 kyr eccentricity cycle is reduced. We linked lowest temperatures to intensified upwelling during precession maxima. However, if the intensity of upwelling depended on the amplitude of precession, we would expect lowest temperatures to occur during eccentricity maxima, which is not the case. Alternatively, the degree of stratification was dependent on the amplitude of precession, resulting in greater stratification and higher temperatures during eccentricity maxima, as observed. This agrees with the increased abundance of dinoflagellate cyst *Polysphaeridium* during TEX_{86} maxima, which indicates extreme stratification of surface waters (hyperstratification; Wubben et al., in press). The temperature sensitivity to one side of the precession cycle indicates that the response was highly non-linear (Figure 11).

The asymmetry of ~100 kyr TEX_{86} cycles prior to the MCO (17.9-17.7 Ma) and the ~60-50 kyr TEX_{86} cycle around 16.76 Ma suggests that SST at Site 959 was affected by high-latitude, glacial processes (Figure 12). This agrees with occurrence of low temperatures during eccentricity minima and obliquity minima (when glacial periods are expected to occur). Asymmetric, sawtooth-shaped cycles are typical for glacial cycles of the Late Pleistocene (Lisiecki & Raymo, 2007) and are also found in the Early Miocene, linked to prolonged ice sheet growth on Antarctica and subsequent rapid retreat (Liebrand et al., 2017). The mostly symmetrical cycles during the MCO indicate a more direct response to astronomical forcing, which is in line with a smaller Antarctic ice sheet that was restricted to the inner continent (Colleoni et al., 2018). However, high-latitude processes might have still contributed to the

pronounced and non-linear (i.e., symmetrical but one-sided) ~100 kyr TEX_{86} signal between 16.5 and 15.0 Ma.

Antarctic terminations presumably occurred in response to austral summer insolation maxima (Holbourn et al., 2013; Holbourn et al., 2014; de Vleeschouwer et al., 2017), suggesting TEX_{86} maxima (which follow the inferred terminations) were related to precession maxima. This is in disagreement with the most likely precession phasing based on monsoon forcing. It is unlikely that the precession phasing of TEX_{86} switched throughout the Early to Middle Miocene, because no significant changes in phasing are observed between TEX_{86} and other proxies. Throughout the 18-15 Ma interval, TEX_{86} maxima remain in phase with $\delta^{13}C$ and $\delta^{18}O$ minima, slightly lagging $\delta^{13}C$ at ~100 kyr scale and leading at precession scale (Figure S12). Potentially, the timing of the TEX_{86} maxima is determined by a combination of monsoonal and glacial forcing. During the late Pleistocene, benthic $\delta^{18}O$ lagged the summer insolation forcing by ~6 kyr for precession (e.g., Konijnendijk et al., 2015), which is half of the duration between precession maxima and minima (~11 kyr), and major deglaciations affected the timing of the African monsoon (~3 kyr lag; e.g., Grant et al., 2016). For the Miocene, it might be possible that major Antarctic deglaciations induced leads in the monsoon response, shifting TEX_{86} maxima towards the timing of ice-volume minima in between the precession extremes. A phase lead with the precession extremes can also be established if TEX_{86} responded to insolation changes earlier in the year than the solstice, resulting in a lead of ~1.8 kyr per month earlier. For example, the SE trade winds, which drive equatorial upwelling, intensify from March to mid-June (Caniaux et al., 2011). Although this might provide an explanation, the precession phasing, which is crucial for understanding the climate system, remains enigmatic.

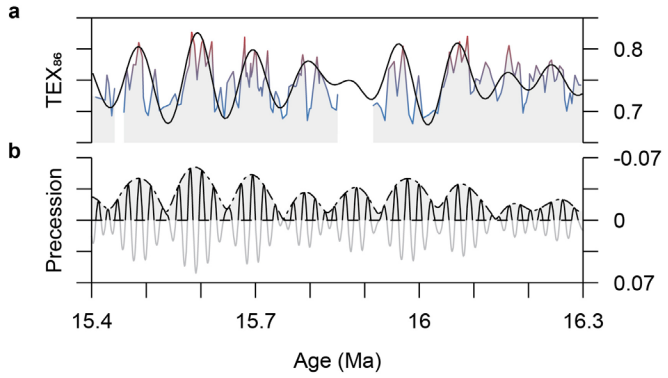

Figure 11. Non-linear TEX_{86} response between 16.3 and 15.4 Ma. The TEX_{86} record is indicated by the red-blue line (representing warmer-colder temperatures) and overlain with its bandpass filter of ~100 kyr cyclicity (black; **a**). The non-linear, one-sided response to precession (solid black/gay) is illustrated by the horizontal dached line. The amplitude of precession is modulated

609 by eccentricity (dashed-dotted black). Precession and eccentricity are derived from the La2004
610 solution (Laskar et al., 2004). See caption of Figure 8 for bandpass filter width.

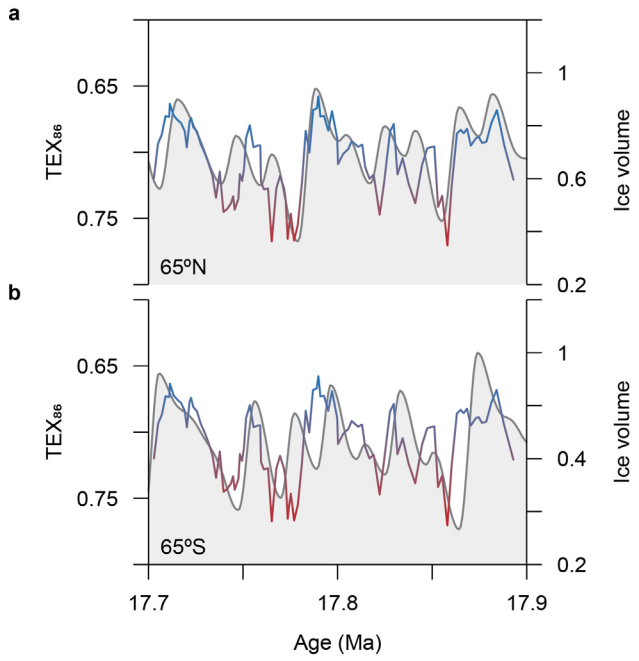

611

612 **Figure 12.** Asymmetric TEX_{86} cycles between 17.9 and 17.7 Ma. The TEX_{86} record is indicated
613 by the red-blue line (representing warmer-colder temperatures) and compared to the ice volume
614 model of Imbrie and Imbrie (1980) using insolation forcing of 65°N June 21 (**a**) and 65°S
615 December 21 (**b**) computed with Astrochron (Meyers, 2014).

616 5.4 Obliquity and high-latitude influence

617 The influence of obliquity is recorded throughout the Early to Middle Miocene (18-15
618 Ma) at Site 959, expressed as ~41 kyr obliquity or as combination tones of precession and
619 obliquity (~60-50 kyr cyclicity). A strong influence of obliquity is recorded prior to the MCO
620 (18.2-17.7 Ma) and just after the onset of the MCO (16.9-16.3 Ma), while the effect of obliquity
621 is expected to be much smaller than that of precession at low latitudes (Bosmans, Drijfhout, et
622 al., 2015; Bosmans, Hilgen, et al., 2015). In insolation curves, the expression of obliquity can
623 become more evident during ~400 kyr and 2.4 Myr eccentricity minima (Figure S13). This can
624 be observed in the TEX_{86} record as an increase in the amplitude of ~41 kyr cyclicity during the
625 ~400 kyr eccentricity minima around 16.2 and 15.8 Ma. Although the 16.9-16.3 Ma interval
626 corresponds to a 2.4 Myr eccentricity minimum, the very pronounced ~60-50 kyr cyclicity
627 suggests that at least part of the obliquity influence must be derived from high-latitudes where
628 insolation is more influenced by obliquity.

629 Benthic $\delta^{18}O$ records indicate that the high-latitude climate was paced by obliquity and
630 eccentricity during the Early Miocene (Billups et al., 2004; Liebrand et al., 2016; Liebrand et al.,
631 2017; Pälike et al., 2006) and mainly by ~100 kyr eccentricity during the Middle to Late
632 Miocene, with a switch to dominant obliquity pacing during 2.4 Myr eccentricity minima around
633 14.4, 9.5, and 7.5 Ma (Holbourn et al., 2007; Holbourn et al., 2018). Although direct comparison
634 is difficult, this seems to agree with patterns reflected in the Lower to Middle Miocene proxy

635 records of Site 959 (Figure S14). High-latitude, glacial-interglacial variability (on both
636 eccentricity and obliquity scales) could have been transferred to the tropics through changes in
637 oceanic circulation, atmospheric circulation and/or greenhouse gases. Differences in the
638 contribution of high- and low-latitude processes might have caused the differences in variability
639 between the proxies, while the differences through time resulted from the influence of the 2.4
640 Myr eccentricity cycle on insolation forcing.

641 5.4.1 Ocean circulation

642 Late Pliocene TEX_{86} at Site 959, although representing a deeper signal, was also sensitive
643 to glacial-interglacial variability and minima concurred with glacial stages (van der Weijst et al.,
644 2022). Sub-thermocline waters at Site 959 are delivered by South Atlantic Central Water
645 (SACW), which mixes at depth with Antarctic Intermediate Water (AAIW; van der Weijst et al.,
646 2022). Similar to simulations for the Eocene-Oligocene transition, meridional overturning
647 circulation and northward transport of AAIW might have been enhanced in response to Antarctic
648 ice sheet growth (Goldner et al., 2014). This might have decreased the temperature of upwelled
649 water at Site 959.

650 5.4.2 Atmospheric circulation

651 Additionally, colder periods on Antarctica might have intensified trade winds. For the
652 bipolar-glaciated Pleistocene, both simulation and proxy data indicate intensification of NE trade
653 winds during colder periods in the northern hemisphere (McGee et al., 2018). Oppositely, an
654 intensification of SE trade winds has been recorded in the southeastern Atlantic during Antarctic
655 cold periods over the last 135 kyr (Shi et al., 2001) and during Antarctic ice volume increases
656 during the Middle to Late Miocene (Heinrich et al., 2011). As SE trade winds drive the Atlantic
657 cold tongue (Caniaux et al., 2011), their intensification might result in lower temperatures in the
658 eastern equatorial Atlantic. As suggested for the obliquity-paced early Pleistocene icehouse,
659 glacial intensification of trade winds might result in a tight coupling between SST and
660 productivity in equatorial upwelling regions (Cleaveland & Herbert, 2007). This could explain
661 the concurrence of high Ba_{bio} peaks with pronounced TEX_{86} minima at Site 959. After the onset
662 of the MCO (16.9-16.3 Ma), the hypothesized glacial periods also concurred with Ti/Al peaks.
663 Possibly, large-scale changes in atmospheric circulation related to high-latitude cooling also led
664 to decreased West African rainfall. This had been suggested for the strong correlation between
665 riverine input east of Site 959 and northern high latitude climate over the past 155 kyr (Weldeab
666 et al., 2007), but it is not clear if Antarctic climate change would have a similar effect.

667 5.4.3 Greenhouse gases

668 Lastly, glacial-interglacial variations in greenhouse gases could have affected the tropical
669 climate. Simulations show that elevated atmospheric CO_2 concentrations result in overall higher
670 SSTs, enhancing the Atlantic ITCZ and African monsoon precipitation (Acosta et al., 2022).
671 Therefore, lowered atmospheric CO_2 concentrations during glacial periods could have resulted in
672 increased North African aridity and dust supply to Site 959. The strong and nearly synchronous
673 response of tropical SSTs to obliquity during the Early Pleistocene was also attributed to glacial-
674 interglacial greenhouse gas forcing (Cleaveland & Herbert, 2007). This indicates that the high-
675 latitude influence on the tropics was strong even though the northern hemisphere ice sheets were
676 still relatively small, which could be similar for the southern hemisphere ice sheets of the Early
677 to Middle Miocene.

6 Conclusions

Early to Middle Miocene proxy records from Site 959 provide insights into astronomically-forced tropical climate dynamics across the prelude, onset, and continuation of the MCO (18-15 Ma). Maxima of $\delta^{13}C$ generally correspond to maxima of $\delta^{18}O$, Ba_{bio}, Ti/Al, and V/Al, minima of wt% $CaCO_3$ and TEX_{86}, and darker sediment layers which are likely rich in biogenic silica. The records revealed periodicities of ~400 and ~100 kyr, ~41 kyr, and ~27-17 kyr which are likely related to ~400 and ~100 kyr eccentricity, obliquity, and precession, respectively, and ~60-50 kyr cyclicity related to combination tones of precession and obliquity. Variability differed between proxy records and, mainly for TEX_{86}, changed through time in three distinct phases: (1) strong eccentricity, obliquity and precession variability prior to the MCO (18.2-17.7 Ma), (2) strong influence of obliquity just after the onset of the MCO (16.9-16.3 Ma) occurring within a 2.4 Myr eccentricity minimum, and (3) dominant eccentricity and precession variability between 16.3 and 15.0 Ma. Monsoon dynamics induced changes in upwelling intensity and North African aridity, resulting in low SSTs (TEX_{86}) coinciding with high productivity (Ba_{bio}) and dust input (Ti/Al) at Site 959. Because of asymmetry and strong obliquity influence, it is considered likely that Site 959 was also affected by high-latitude, glacial-interglacial variability throughout the Early to Middle Miocene. Therefore, Site 959 proxy records are interpreted to reflect a complex system that was sensitive to seasonality, low-latitude insolation forcing, and high-latitude dynamics.

Acknowledgments

This work was funded by the European Research Council (Consolidator Grant 771497, awarded to Appy Sluijs) under the Horizon 2020 program. We thank Coen Mulder (Utrecht University) for technical support. We thank Joyce Bosmans for sharing her unpublished model results.

Conflict of Interest

The authors declare that they have no conflict of interest.

Open Research

The data presented in this study, including those of Wubben et al. (2023) and Wubben et al. (in press), are available at Zenodo (Sluijs et al., 2023).

References

Acosta, R. P., Ladant, J.-B., Zhu, J., & Poulsen, C. J. (2022). Evolution of the Atlantic Intertropical Convergence Zone, and the South American and African monsoons over the past 95-Myr and their impact on the tropical rainforests. *Paleoceanography and Paleoclimatology*, *37*(7), e2021PA004383. https://doi.org/10.1029/2021PA004383

Basile, C., Mascle, J., Popoff, M., Bouillin, J. P., & Mascle , G. (1993). The Ivory Coast-Ghana transform margin: A marginal ridge structure deduced from seismic data. *Tectonophysics*, *222*(1), 1-19. https://doi.org/10.1016/0040-1951(93)90186-N

Beckmann, B., Flögel, S., Hofmann, P., Schulz, M., & Wagner, T. (2005). Orbital forcing of Cretaceous river discharge in tropical Africa and ocean response. *Nature*, *437*, 241-244. https://doi.org/10.1038/nature03976

Beddow, H. M., Liebrand, D., Wilson, D. S., Hilgen, F. J., Sluijs, A., Wade, B. S., & Lourens, L. J. (2018). Astronomical tunings of the Oligocene-Miocene transition from Pacific Ocean Site U1334 and implications for the carbon cycle. *Climate of the Past*, *14*(3), 255-270. https://doi.org/10.5194/cp-14-255-2018

Behrooz, L., Naafs, B. D. A., Dickson, A. J., Love, G. D., Batenburg, S. J., & Pancost, R. D. (2018). Astronomically driven variatons in depositional environments in the South Atlantic during the Early Cretaceous. *Paleoceanography and Paleoclimatology, 33*, 894-912. https://doi.org/10.1029/2018PA003338

Billups, K., Pälike, H., Channell, J. E. T., Zachos, J. C., & Shackleton, N. J. (2004). Astronomic calibration of the Late Oligocene through Early Miocene geomagnetic polarity time scale. *Earth and Planetary Science Letters*, *224*(1-2), 33-44. https://doi.org/10.1016/j.epsl.2004.05.004

732 Bosmans, J. H. C., Drijfhout, S. S., Tuenter, E., Hilgen, F. J., & Lourens, L. J. (2015). Response
733 of the North African summer monsoon to precession and obliquity forcings in the EC-Earth
734 GCM. *Climate Dynamics, 44*, 279-297. https://doi.org/10.1007/s00382-014-2260-z
735 Bosmans, J. H. C., Hilgen, F. J., Tuenter, E., & Lourens, L. J. (2015). Obliquity forcing of low-
736 latitude climate. *Climate of the Past, 11*(10), 1335-1346. https://doi.org/10.5194/cp-11-1335-
737 2015
738 Burls, N. J., Bradshaw, C. D., de Boer, A. M., Herold, N., Huber, M., Pound, M., Donnadieu, Y.,
739 Farnsworth, A., Frigola, A., Gasson, E., von der Heydt, A. S., Hutchinson, D. K., Knorr, G.,
740 Lawrence, K. T., Lear, C. H., Li, X., Lohmann, G., Lunt, D. J., Marzocchi, A., Prange, M.,
741 Riihimaki, C. A., Sarr, A.-C., Siler, N., & Zhang, Z. (2021). Simulating Miocene warmth:
742 Insights from an opportunistic multi-model ensemble (MioMIP1). *Paleoceanography and*
743 *Paleoclimatology, 36*(5), 1-40. https://doi.org/10.1029/2020PA004054
744 Calvert, S. E., & Pedersen, T. F. (2007). Chapter fourteen elemental proxies for palaeoclimatic
745 and palaeoceanographic variability in marine sediments: Interpretation and application.
746 *Developments in Marine Geology, 1*, 567-644. https://doi.org/10.1016/S1572-5480(07)01019-6
747 Caniaux, G., Giordani, H., Redelsperger, J.-L., Guichard, F., Key, E., & Wade, M. (2011).
748 Coupling between the Atlantic cold tongue and the West African monsoon in boreal spring and
749 summer. *Journal of Geophysical Research, 116*, C04003. https://doi.org/10.1029/2010JC006570
750 Cleaveland, L. C., & Herbert, T. D. (2007). Coherent obliquity band and heterogenous
751 precession band responses in early Pleistocene tropical sea surface temperatures.
752 *Paleoceanography, 22*(2), PA2216. https://doi.org/10.1029/2006PA001370
753 Colleoni, F., de Santis, L., Montoli, E., Olivo, E., Sorlien, C. C., Bart, P. J., Gasson, E. G. W.,
754 Bergamasco, A., Sauli, C., Wardell, N., & Prato, S. (2018). Past continental shelf evolution

755 increased Antarctic ice sheet sensitivity to climatic conditions. *Scientific Reports, 8*, 11323.
756 https://doi.org/10.1038/s41598-018-29718-7
757 Cramwinckel, M. J., Huber, M., Kocken, I. J., Agnini, C., Bijl, P. K., Bohaty, S. M., Frieling, J.,
758 Goldner, A., Hilgen, F. J., Kip, E. L., Peterse, F., van der Ploeg, R., Röhl, U., Schouten, S., &
759 Sluijs, A. (2018). Synchronous tropical and polar temperature evolution in the Eocene. *Nature,*
760 *559*, 382-386. https://doi.org/10.1038/s41586-018-0272-2
761 Crocker, A. J., Naafs, B. D. A., Westerhold, T., James, R. H., Cooper, M. J., Röhl, U., Pancost,
762 R. D., Xuan, C., Osborn, C. P., Beerling, D. J., & Wilson, P. A. (2022). Astronomically
763 controlled aridity in the Sahara since at least 11 million years ago. *Nature Geoscience, 15*, 671-
764 676. https://doi.org/10.1038/s41561-022-00990-7
765 DeMenocal, P. B. (2004). African climate change and faunal evolution during the Pliocene-
766 Pleistocene. *Earth and Planetary Science Letters, 220*(1-2), 3-24. https://doi.org/10.1016/S0012-
767 821X(04)00003-2
768 De Vleeschouwer, D., Vahlenkamp, M., Crucifix, M., & Pälike, H. (2017). Alternating southern
769 and northern hemisphere climate response to astronomical forcing during the past 35 m.y.
770 *Geology, 45*(4), 375-378. https://doi.org/10.1130/G38663.1
771 Djakouré, S., Penven, P., Bourlès, B., Koné, V., & Veitch, J. (2017). Respective roles of the
772 Guinea Current and local winds on the coastal upwelling in the northern Gulf of Guinea. *Journal*
773 *of Physical Oceanography, 47*(6), 1367-1387. https://doi.org/10.1175/JPO-D-16-0126.1
774 Droz, L., Blarez, E., Mascle, J., & Boko, S. (1985). The Trou Sans Fond deep-sea fan (off Ivory
775 Coast, equatorial Atlantic). *Marine Geology, 67*(1-2), 1-11. https://doi.org/10.1016/0025-
776 3227(85)90145-8

777 Dymond, J., Suess, E., & Lyle, M. (1992). Barium in deep-sea sediment: A geochemical proxy
778 for paleoproductivity. *Paleoceanography, 7*(2), 163-181. https://doi.org/10.1029/92PA00181
779 Foster, G. L., Lear, C. H., & Rae, J. W. B. (2012). The evolution of pCO_2, ice volume and
780 climate during the Middle Miocene. *Earth and Planetary Science Letters, 341-344*, 243-254.
781 https://doi.org/10.1016/j.epsl.2012.06.007
782 Frieling, J., Peterse, F., Lunt, D. J., Bohaty, S. M., Sinninghe Damsté, J. S., Reichart, G.-J., &
783 Sluijs, A. (2019). Widespread warming before and elevated barium burial during the Paleocene-
784 Eocene Thermal Maximum: Evidence for methane hydrate release? *Paleoceanography and*
785 *Paleoclimatology, 34*(4), 546-566. https://doi.org/10.1029/2018PA003425
786 GEBCO Bathymetric Compilation Group (2022). The GEBCO_2022 Grid – A continuous
787 terrain model of the global ocean and land. *British Oceanographic Data Centre*.
788 https://doi.org/10.5285/e0f0bb80-ab44-2739-e053-6c86abc0289c
789 Goldner, A., Herold, N., & Huber, M. (2014). Antarctic glaciation caused ocean circulation
790 changes at the Eocene-Oligocene transition. *Nature, 511*, 574-577.
791 https://doi.org/10.1038/nature13597
792 Govin, A., Holzwarth, U., Heslop, D., Ford Keeling, L., Zabel, M., Mulitza, S., Collins, J. A., &
793 Chiessi, C. M. (2012). Distribution of major elements in Atlantic surface sediments (36°N-49°S):
794 Imprint of terrigenous input and continental weathering. *Geochemistry, Geophysics, Geosystems,*
795 *13*(1), 1-23. https://doi.org/10.1029/2011GC003785
796 Grant, K. M., Grimm, R., Mikolajewicz, U., Marino, G., Ziegler, M., & Rohling, E. J. (2016).
797 The timing of Mediterranean sapropel deposition relative to insolation, sea-level and African
798 monsoon changes. *Quaternary Science Reviews, 140*, 125-141.
799 https://doi.org/10.1016/j.quascirev.2016.03.026

800 Heinrich, S., Zonneveld, K. A. F., Bickert, T., & Willems, H. (2011). The Benguela upwelling
801 related to the Miocene cooling events and the development of the Antarctic Circumpolar
802 Current: Evidence from calcareous dinoflagellate cysts. *Paleoceanography, 26*(3), PA3209.
803 https://doi.org/10.1029/2010PA002065
804 Hinnov, L. A. (2013). Cyclostratigraphy and its revolutionizing applications in the earth and
805 planetary sciences. *Geological Society of America Bulletin, 125*(11-12), 1703-1734.
806 https://doi.org/10.1130/B30934.1
807 Holbourn, A., Kuhnt, W., Schulz, M., Flores, J. A., & Andersen, N. (2007). Orbitally-paced
808 climate evolution during the middle Miocene Monterey carbon-isotope excursion. *Earth and*
809 *Planetary Science Letters, 261*(3-4), 534-550. https://doi.org/10.1016/j.epsl.2007.07.026
810 Holbourn, A., Kuhnt, W., Lyle, M., Schneider, L., Romero, O., & Andersen, N. (2014). Middle
811 Miocene climate cooling linked to intensification of eastern equatorial Pacific upwelling.
812 *Geology, 42*(1), 19-22. https://doi.org/10.1130/G34890.1
813 Holbourn, A., Kuhnt, W., Clemens, S., Prell, W., & Andersen, N. (2013). Middle to Late
814 Miocene stepwise climate cooling: Evidence from a high-resolution deep water isotope curve
815 spanning 8 million years. *Paleoceanography, 28*(4), 688-699.
816 https://doi.org/10.1002/2013PA002538
817 Holbourn, A. E., Kuhnt, W., Clemens, S. C., Kochhann, K. G. D., Jöhnck, J., Lübbers, J., &
818 Andersen, N. (2018). Late Miocene climate cooling and intensification of southeast Asian winter
819 monsoon. *Nature Communications, 9*, 1584. https://doi.org/10.1038/s41467-018-03950-1
820 Holbourn, A., Kuhnt, W., Kochhann, K. G. D., Andersen, N., & Meier, K. J. S. (2015). Global
821 perturbation of the carbon cycle at the onset of the Miocene Climatic Optimum. *Geology, 43*(2),
822 123-126. https://doi.org/10.1130/G36317.1

Hopmans, E. C., Weijers, J. W. H., Schefuß, E., Herfort, L., Sinninghe Damsté, J. S., & Schouten, S. (2004). A novel proxy for terrestrial organic matter in sediments based on branched and isoprenoid tetraether lipids. *Earth and Planetary Science Letters, 224*(1-2), 107-116. https://doi.org/10.1016/j.epsl.2004.05.012

Hounslow, M. W., White, H. E., Drake, N. A., Salem, M. J., El-Hawat, A., McLaren, S. J., Karloukovski, V., Noble, S. R., & Hlal, O. (2017). Miocene humid intervals and establishment of drainage networks by 23 Ma in the central Sahara, southern Libya. *Gondwana Research, 45*, 118-137. https://doi.org/10.1016/j.gr.2016.11.008

Imbrie, J., & Imbrie, J. Z. (1980). Modeling the climatic response to orbital variations. *Science, 207*(4434), 943-953. https://doi.org/10.1126/science.207.4434.943

Kasten, S., Haese, R. R., Zabel, M., Ruhlemann, C., & Schulz, H. D. (2001). Barium peaks at glacial terminations in sediments of the equatorial Atlantic Ocean – relicts of deglacial productivity pulses? *Chemical Geology, 175*(3-4), 635-651. https://doi.org/10.1016/S0009-2541(00)00377-6

Konijnendijk, T. Y. M., Ziegler, M., & Lourens, L. J. (2014). Chronological constraints on Pleistocene sapropel depositions from high-resolution geochemical records of ODP Sites 967 and 968. *Newsletters on Stratigraphy, 47*(3), 263-282. https://doi.org/10.1127/0078-0421/2014/0047

Konijnendijk, T. Y. M., Ziegler, M., & Lourens, L. J. (2015). On the timing and forcing mechanisms of late Pleistocene glacial terminations: Insights from a new high-resolution benthic stable oxygen isotope record of the eastern Mediterranean. *Quaternary Science Reviews, 129*, 308-320. https://doi.org/10.1016/j.quascirev.2015.10.005

Larrasoaña, J. C., Roberts, A. P., Rohling, E. J., Winklhofer, M., & Wehausen, R. (2003). Three million years of monsoon variability over the northern Sahara. *Climate Dynamics, 21*, 689-698. https://doi.org/10.1007/s00382-003-0355-z

Laskar, J., Robutel, P., Joutel, F., Gastineau, M., Correira, A. C. M., & Levrard, B. (2004). A long-term numerical solution for the insolation quantities of the Earth. *Astronomy & Astrophysics, 428*(1), 261-285. https://doi.org/10.1051/0004-6361:20041335

Li, M., Hinnov, L., & Kump, L. (2019). Acycle: Time-series analysis software for paleoclimate research and education. *Computers and Geosciences, 127*, 12-22. https://doi.org/10.1016/j.cageo.2019.02.011

Liebrand, D., Beddow, H. M., Lourens, L. J., Pälike, H., Raffi, I., Bohaty, S. M., Hilgen, F. J., Saes, M. J. M., Wilson, P. A., van Dijk, A. E., Hodell, D. A., Kroon, D., Huck, C. E., & Batenburg, S. J. (2016). Cyclostratigraphy and eccentricity tuning of the Early Oligocene through Early Miocene (30.1-17.1 Ma): Cibicides mundulus stable oxygen and carbon isotope records from Walvis Ridge Site 1264. *Earth and Planetary Science Letters, 450*, 392-405. https://doi.org/10.1016/j.epsl.2016.06.007

Liebrand, D., de Bakker, A. T. M., Beddow, H. M., Wilson, P. A., Bohaty, S. M., Ruessink, G., Pälike, H., Batenburg, S. J., Hilgen, F. J., Hodell, D. A., Huck, C. E., Kroon, D., Raffi, I., Saes, M. J. M., van Dijk, A. E., & Lourens, L. J. (2017). Evolution of the early Antarctic ice ages. *Proceedings of the National Academy of Sciences of the United States of America, 114*(15), 3867-3872. https://doi.org/10.1073/pnas.1615440114

Lisiecki, L. E., & Raymo, M. E. (2007). Plio-Pleistocene climate evolution: Trends and transitions in glacial cycle dynamics. *Quaternary Science Reviews, 26*(1-2), 56-69. https://doi.org/10.1016/j.quascirev.2006.09.005

868 Lourens, L. J., Wehausen, R., & Brumsack, H. J. (2001). Geological constraints on tidal
869 dissipation and dynamical ellipticity of the Earth over the past three million years. *Nature, 409*,
870 1029-1033. https://doi.org/10.1038/35059062
871 Martinez-Ruiz, F., Kastner, M., Gallego-Torres, D., Rodrigo-Gámiz, M., Nieto-Moreno, V., &
872 Ortega-Huertas, M. (2015). Paleoclimate and paleoceanography over the past 20,000 yr in the
873 Mediterranean Sea basins as indicated by sediment elemental proxies. *Quaternary Science*
874 *Reviews, 107*(1), 25-46. https://doi.org/10.1016/j.quascirev.2014.09.018
875 Mascle, J., Lohmann, G. P., Clift, P. D., Akamaluk, T., Allerton, S., Ask, M. V. S., et al. (1996).
876 *Proceedings of the Ocean Drilling Program, Initial Reports* (Vol. 159). College Station, TX:
877 Ocean Drilling Program.
878 McGee, D., Moreno-Chamarro, E., Green, B., Marshall, J., Galbraith, E., & Bradtmiller, L.
879 (2018). Hemispherically asymmetric trade wind changes as signatures of past ITCZ shifts.
880 *Quaternary Science Reviews, 180*, 214-228. https://doi.org/10.1016/j.quascirev.2017.11.020
881 McIntyre, A., Ruddiman, W. F., Karlin, K., & Mix, A. C. (1989). Surface water response of the
882 equatorial Atlantic Ocean to orbital forcing. *Paleoceanography and Paleoclimatology, 4*(1), 19-
883 55. https://doi.org/10.1029/PA004i001p00019
884 Meyers, S. R. (2012). Seeing red in cyclic stratigraphy: Spectral noise estimation for
885 astrochronology. *Paleoceanography, 27*(3), PA3328. https://doi.org/10.1029/2012PA002307
886 Meyers, S. R. (2014). Astrochron: An R package for astrochronology. https://cran.r-
887 project.org/package=astrochron
888 Müller, R. D., Cannon, J., Qin, X., Watson, R. J., Gurnis, M., Williams, S., Pfaffelmoser, T.,
889 Seton, M., Russell, S. H. J., & Zahirovic, S. (2018). GPlates: Building a virtual Earth through

deep time. *Geochemistry, Geophysics, Geosystems, 19*(7), 2243-2261. https://doi.org/10.1029/2018GC007584

Norris, R. D. (1998a). Miocene-Pliocene surface-water hydrography of the eastern equatorial Atlantic. In J. Mascle, G. P. Lohmann, & M. Moullade (Eds.), *Proceedings of the Ocean Drilling Program, Scientific Results* (Vol. 159, pp. 539-555). College Station, TX: Ocean Drilling Program.

Norris, R. D. (1998b). Planktonic foraminifer biostratigraphy: Eastern equatorial Atlantic. In J. Mascle, G. P. Lohmann, & M. Moullade (Eds.), *Proceedings of the Ocean Drilling Program, Scientific Results* (Vol. 159, pp. 445-479). College Station, TX: Ocean Drilling Program.

O'Mara, N. A., Skonieczny, C., McGee, D., Winckler, G., Bory, A., J.-M., Bradtmiller, L. I., Malaizé, B., & Polissar, P. J. (2022). Pleistocene drivers of northwest African hydroclimate and vegetation. *Nature Communications, 13*, 3552. https://doi.org/10.1038/s41467-022-31120-x

Pälike, H., Frazier, J., & Zachos, J. C. (2006). Extended orbitally forced paleoclimatic records from the equatorial Atlantic Ceara Rise. *Quaternary Science Reviews, 25*(23-24), 3138-3149. https://doi.org/10.1016/j.quascirev.2006.02.011

Piela, C., Lyle, M., Marcantonio, F., Baldauf, J., & Olivarez Lyle, A. (2012). Biogenic sedimentation in the equatorial Pacific: Carbon cycling and paleoproduction, 12-24 Ma. *Paleoceanography, 27*(2). https://doi.org/10.1029/2011PA002236

Prospero, J. M., Ginoux, P., Torres, O., Nicholson, S. E., & Gill, T. E. (2002). Environmental characterization of global sources of atmospheric soil dust identified with the Nimbus 7 Total Ozone Mapping Spectrometer (TOMS) absorbing aerosol product. *Reviews of Geophysics, 40*(1), 1002. https://doi.org/10.1029/2000RG000095

912 Reitz, A., Pfeifer, K., de Lange, G. J., & Klump, J. (2004). Biogenic barium and the detrital
913 Ba/Al ratio: A comparison of their direct and indirect determination. *Marine Geology, 204*(3-4),
914 289-300. https://doi.org/10.1016/S0025-3227(04)00004-0
915 Rossignol-Strick, M. (1983). African monsoons, an immediate climate response to orbital
916 insolation. *Nature, 304*, 46-49. https://doi.org/10.1038/304046a0
917 Schenau, S. J., Antonarakou, A., Hilgen, F. J., Lourens, L. J., Nijenhuis, I. A., van der Weijden,
918 C. H., & Zachariasse, W. J. (1999). Organic-rich layers in the Metochia section (Gavdos,
919 Greece): Evidence for a single mechanism of sapropel formation during the past 10 My. *Marine*
920 *Geology, 153*(1-4), 117-135. https://doi.org/10.1016/S0025-3227(98)00086-3
921 Schouten, S., Hopmans, E. C., Schefuß, E., & Sinninghe Damsté, J. S. (2002). Distributional
922 variations in marine crenarchaeotal membrane lipids: A new tool for reconstructing ancient sea
923 water temperatures? *Earth and Planetary Science Letters, 204*(1-2), 265-274.
924 https://doi.org/10.1016/S0012-821X(02)00979-2
925 Seton, M., Müller, R. D., Zahirovic, S., Gaina, C., Torsvik, T., Shephard, G., Talsma, A., Gurnis,
926 M., Turner, M., Maus, S., & Chandler, M. (2012). Global continental and ocean basin
927 reconstructions since 200 Ma. *Earth-Science Reviews, 113*(3-4), 212-270.
928 https://doi.org/10.1016/j.earscirev.2012.03.002
929 Shafik, S., Watkins, D. K., & Chul Shin, I. (1998). Upper Cenozoic calcareous nannofossil
930 biostratigraphy Côte d'Ivoire-Ghana Margin, eastern equatorial Atlantic. In J. Mascle, G. P.
931 Lohmann, & M. Moullade (Eds.), *Proceedings of the Ocean Drilling Program, Scientific Results*
932 (Vol. 159, pp. 509-523). College Station, TX: Ocean Drilling Program.

933 Shi, N., Schneider, R., Beug, H.-J., & Dupont, L. (2001). Southeast trade wind variations during
934 the last 135 kyr: Evidence from pollen spectra in eastern south Atlantic sediments. *Earth and*
935 *Planetary Science Letters, 187*(3-4), 311-321. https://doi.org/10.1016/S0012-821X(01)00267-9
936 Skonieczny, C., McGee, D., Winckler, G., Bory, A., Bradtmiller, L. I., Kinsley, C. W., Polissar,
937 P. J., De Pol-Holz, R., Rossignol, L., & Malaizé, B. (2019). Monsoon-driven Saharan dust
938 variability over the past 240,000 years. *Science Advances, 5*(1).
939 https://doi.org/10.1126/sciadv.aav1887
940 Sluijs, A., Fokkema, C. D., Agterhuis, T., Gerritsma, D., de Goeij, M., Liu, X., de Regt, P., Rice,
941 A., Vennema, L., Agnini, C., Bijl, P. K., Frieling, J., Huber, M., Peterse, F., Wubben, E.,
942 Spiering, B., Veenstra, T., Bos, R., Wang, Z., van Dijk, J., Raffi, I., Witkowski, J., Hilgen, F.,
943 Peterse, F., & Sangiorgi, F. (2023). Ocean Drilling Program Site 959 datasets [Dataset]. Zenodo.
944 https://doi.org/10.5281/zenodo.8309642
945 Sosdian, S. M., Greenop, R., Hain, M. P., Foster, G. L., Pearson, P. N., & Lear, C. H. (2018).
946 Constraining the evolution of Neogene ocean carbonate chemistry using the boron isotope pH
947 proxy. *Earth and Planetary Science Letters, 498*, 362-376.
948 https://doi.org/10.1016/j.epsl.2018.06.017
949 Steinthorsdottir, M., Coxall, H. K., de Boer, A. M., Huber, M., Barbolini, N., Bradshaw, C. D.,
950 Burls, N. J., Feakins, S. J., Gasson, E., Henderiks, J., Holbourn, A. E., Kiel, S., Kohn, M. J.,
951 Knorr, G., Kürschner, W. M., Lear, C. H., Liebrand, D., Lunt, D. J., Mörs, T., Pearson, P. N.,
952 Pound, M. J., Stoll, H., & Strömberg, C. A. E. (2021). The Miocene: The future of the past.
953 *Paleoceanography and Paleoclimatology, 36*(4), e2020PA004037.
954 https://doi.org/10.1029/2020PA004037

Steinthorsdottir, M., Vajda, V., & Pole, M. (2019). Significant transient pCO_2 perturbation at the New Zealand Oligocene-Miocene transition recorded by fossil plant stomata. *Palaeogeography, Palaeoclimatology, Palaeoecology, 515*, 152-161. https://doi.org/10.1016/j.palaeo.2018.01.039

Stoll, H. M., Guitian, J., Hernandez-Almeida, I., Mejia, M., Phelps, S., Polissar, P., Rosenthal, Y., Zhang, H., & Ziveri, P. (2019). Upregulation of phytoplankton carbon concentrating mechanisms during low CO_2 glacial periods and implications for the phytoplankton pCO_2 proxy. *Quaternary Science Reviews, 208*, 1-20. https://doi.org/10.1016/j.quascirev.2019.01.012

Stuut, J. B., Zabel, M., Ratmeyer, V., Helmke, P., Schefuß, E., Lavik, G., & Schneider, R. (2005). Provenance of present-day eolian dust collected off NW Africa. *Journal of Geophysical Research: Atmospheres, 110*, D04202. https://doi.org/10.1029/2004JD005161

Super, J. R., Thomas, E., Pagani, M., Huber, M., O'Brien, C., & Hull, P. M. (2018). North Atlantic temperature and pCO_2 coupling in the early-middle Miocene. *Geology, 46*(6), 519-522. https://doi.org/10.1130/G40228.1

Thomson, D. J. (1982). Spectrum estimation and harmonic analysis. *Proceedings of the IEEE, 70*(9), 1055-1096. https://doi.org/10.1109/PROC.1982.12433

Tiedemann, R., Sarnthein, M., & Shackleton, N. J. (1994). Astronomic timescale for the Pliocene Atlantic $\delta^{18}O$ and dust flux records of Ocean Drilling Program Site 659. *Paleoceanography, 9*(4), 619-638. https://doi.org/10.1029/94PA00208

Torsvik, T. H., van der Voo, R., Preeden, U., Mac Niocaill, C., Steinberger, B., Doubrovine, P. V., van Hinsbergen, D. J. J., Domeier, M., Gaina, C., Tohver, E., Meert, J.G., McClausland, P. J. A., & Cocks, L. R. M. (2012). Phanerozoic polar wander, paleogeography and dynamics. *Earth-Science Reviews, 114*(3-4), 325-368. https://doi.org/10.1016/j.earscirev.2012.06.007

977 Trauth, M. H., Larrasoaña, J. C., & Mudelsee, M. (2009). Trends, rhythms and events in Plio-
978 Pleistocene African climate. *Quaternary Science Reviews, 28*(5-6), 399-411.
979 https://doi.org/10.1016/j.quascirev.2008.11.003
980 Vallé, F., Westerhold, T., & Dupont, L. M. (2017). Orbital-driven environmental changes
981 recorded at ODP Site 959 (eastern equatorial Atlantic) from the Late Miocene to the Early
982 Pleistocene. *International Journal of Earth Sciences, 106*, 1161-1174.
983 https://doi.org/10.1007/s00531-016-1350-z
984 Van der Weijst, C. M. H., Winkelhorst, J., Lourens, L., Raymo, M. E., Sangiorgi, F., & Sluijs, A.
985 (2020). A ternary mixing model approach using benthic foraminifer $\delta^{13}C$- $\delta^{18}O$ data to
986 reconstruct Late Pliocene deep Atlantic water mass mixing. *Paleoceanography and*
987 *Paleoclimatology, 35*(12), e2019PA003804. https://doi.org/10.1029/2019PA003804
988 Van der Weijst, C. M. H., van der Laan, K. J., Peterse, F., Reichart, G.-J., Sangiorgi, F.,
989 Schouten, S., Veenstra, T. J. T., & Sluijs, A. (2022). A 15-million-year surface- and subsurface-
990 integrated TEX_{86} temperature record from the eastern equatorial Atlantic. *Climate of the Past,*
991 *18*(8), 1947-1962. https://doi.org/10.5194/cp-18-1947-2022
992 Vincent, E., & Berger, W. H. (1985). Carbon dioxide and polar cooling in the Miocene: The
993 Monterey hypothesis. In E. T. Sundquist, & W. S. Broecker (Eds.), *The Carbon Cycle and*
994 *Atmospheric CO2: Natural Variations Archean to Present* (Vol. 32, pp. 455-468). Washington,
995 DC: American Geophysical Union. https://doi.org/10.1029/GM032p0455
996 Von Dobeneck, T., & Schmieder, F. (1999). Using rock magnetic proxy records for orbital
997 tuning and extended time series analyses into the super- and sub-Milankovitch bands. In G.
998 Fischer, & G. Wefer (Eds.), *Use of proxies in paleoceanography* (pp. 601-633). Berlin,
999 Heidelberg: Springer. https://doi.org/10.1007/978-3-642-58646-0_25

1000 Wagner, T. (1998). Pliocene-Pleistocene deposition of carbonate and organic carbon at Site 959:
1001 Paleoenvironmental implications for the eastern equatorial Atlantic off the Ivory Coast/Ghana. In
1002 J. Mascle, G. P. Lohmann, & M. Moullade (Eds.), *Proceedings of the Ocean Drilling Program,*
1003 *Scientific Results* (Vol. 159, pp. 557-574). College Station, TX: Ocean Drilling Program.
1004 Wagner, T. (2002). Late Cretaceous to early Quaternary organic sedimentation in the eastern
1005 equatorial Atlantic. *Palaeogeography, Palaeoclimatology, Palaeoecology, 179*(1-2), 113-147.
1006 https://doi.org/10.1016/S0031-0182(01)00415-1
1007 Wang, P. (2009). Global monsoon in a geological perspective. *Chinese Science Bulletin, 54*,
1008 1113-1136. https://doi.org/10.1007/s11434-009-0169-4
1009 Weijers, J. W. H., Schouten, S., Spaargaren, O. C., & Sinninghe Damsté, J. S. (2006).
1010 Occurrence and distribution of tetraether membrane lipids in soils: Implications for the use of the
1011 TEX_{86} proxy and the BIT index. *Organic Geochemistry, 37*(12), 1680-1693.
1012 https://doi.org/10.1016/j.orggeochem.2006.07.018
1013 Weldeab, S., Lea, D. W., Schneider, R. R., & Andersen, N. (2007). 155,000 years of West
1014 African monsoon and ocean thermal evolution. *Science, 316*(5829), 1303-1307.
1015 https://doi.org/10.1126/science.1140461
1016 Westerhold, T., Marwan, N., Drury, A. J., Liebrand, D., Agnini, C., Anagnostou, E., Barnet, J. S.
1017 K., Bohaty, S. M., de Vleeschouwer, D., Florindo, F., Frederichs, T., Hodell, D. A., Holbourn, A.
1018 E., Kroon, D., Lauretano, V., Littler, K., Lourens, L. J., Lyle, M., Pälike, H., Röhl, U., Tian, J.,
1019 Wilkens, R. H., Wilson, P. A., & Zachos, J. C. (2020). An astronomically dated record of Earth's
1020 climate and its predictability over the last 66 million years. *Science, 369*(6509), 1383-1387.
1021 https://doi.org/10.1126/science.aba6853

Woodruff, F., & Savin, S. M. (1991). Mid-Miocene isotope stratigraphy in the deep sea: High-resolution correlations, paleoclimatic cycles, and sediment preservation. *Paleoceanography and Paleoclimatology, 6*(6), 755–806. https://doi.org/10.1029/91PA02561

Wubben, E., Spiering, B., Veentra, T., Bos, R., Wang, Z., van Dijk, J., Raffi, I., Witkowski, J., Hilgen, F., Peterse, F., Sangiorgi, F., & Sluijs, A. (in press). Tropical warming and intensification of the West African monsoon during the Miocene Climatic Optimum. Submitted to *Paleoceanography and Paleoclimatology* as companion paper.

Wubben, E., Veenstra, T., Witkowski, J., Raffi, I., Hilgen, F., Bos, R., van Dijk, J., Lathouwers, Y., Spiering, B., Vennema, L., Wang, Z., Sangiorgi, F., & Sluijs, A. (2023). Astrochronology of the Miocene Climatic Optimum record from Ocean Drilling Program Site 959 in the eastern equatorial Atlantic. *Newsletters on Stratigraphy, 56*(4), 457-484. https://doi.org/10.1127/nos/2023/0749

Zeebe, R. E., & Lourens, L. J. (2022). A deep-time dating tool for paleo-applications utilizing obliquity and precession cycles: The role of dynamical ellipticity and tidal dissipation. *Paleoceanography and Paleoclimatology, 37*, e2021PA004349. https://doi.org/10.1029/2021PA004349

Zhang, Y. G., Pagani, M., Liu, Z., Bohaty, S. M., & DeConto, R. (2013). A 40-million-year history of atmospheric CO_2. *Philosophical Transactions of the Royal Society A, 371*, 20130096. https://doi.org/10.1098/rsta.2013.0096

Zhang, Z., Ramstein, G., Schuster, M., Li, C., Contoux, C., & Yan, Q. (2014). Aridification of the Sahara desert caused by Tethys Sea shrinkage during the Late Miocene. *Nature, 513*, 401-404. https://doi.org/10.1038/nature13705